Collisional-Radiative Modeling Behind Shock Waves in Nitrogen

Julien Annaloro, Arnaud Bultel, Pierre Omaly

Collisional-Radiative Modeling Behind Shock Waves in Nitrogen

Julien Annaloro* and Arnaud Bultel†
Normandie Université, 76800 Saint-Etienne du Rouvray, France
and
Pierre Omaly‡
Centre National d'Etudes Spatiales, 31401 Toulouse, France

Nonequilibrium plasma, produced by the propagation of a shock wave in a shock tube or behind a shock front detached from a body entering a planetary atmosphere, requires the development of state-to-state models. The collisional-radiative model for N_2 has been elaborated on in this framework for pure nitrogen flows. Its elaboration is reported in this paper. The model includes N_2, N_2^+, N, N^+, and free electrons in thermochemical nonequilibrium. The model is vibrationally and electronically specific insofar as the vibrational states of the electronic ground state of N_2 and the electronic excited states of N_2; and the electronic ground and excited states of N_2^+, N, and N^+ are individually treated. These states are involved in collisional and radiative elementary processes, forming a set of around 40,000 basic data. This model is implemented in a one-dimensional flow, numerical code based on an Eulerian approach. Two test cases are treated at Mach numbers of around 30 and 40, the conditions of which relate to the reentry experiment of the Flight Investigation of Reentry Environment II probe. The behavior of the species on their different states is described in detail. It is shown that the vibrational distribution departs from the Boltzmann equilibrium. The global dissociation and ionization phases of the flow are examined by analyzing the source term for N ground state and electron densities. The radiative losses do not play a significant role in the present conditions.

Nomenclature

A	=	constant of the preexponential factor in the modified Arrhenius law $[k]$, $K^{-\alpha}$
A_{ji}	=	Einstein coefficient, s^{-1}
a_0	=	first Bohr radius, m
a_1, a_2	=	rate coefficient nondimensional parameters
B	=	activation temperature in the modified Arrhenius law, K
b	=	cross-section nondimensional parameter
D_d	=	dissociation degree
D_i	=	ionization degree
E_d	=	dissociation energy, eV
E_v	=	energy of the vibrational state v of $N_2(X)$, eV
$e_A, e_e, \ldots$	=	internal energy per unit volume, $J \cdot m^{-3}$
f_{ij}	=	mean absorption oscillator strength
g	=	statistical weight
i, j	=	excited state
k	=	rate coefficient, $m^3 \cdot s^{-1}$ or $m^6 \cdot s^{-1}$
k_B	=	Boltzmann constant, $J \cdot K^{-1}$
k_v	=	vibrationally specific rate coefficient, $m^3 \cdot s^{-1}$ or $m^6 \cdot s^{-1}$
$\mathscr{M}$	=	Mach number in downstream flow, where x is greater than 0
$\mathscr{M}_0$	=	Mach number in upstream flow, where x is less than 0
m	=	numbers of the elementary processes involved in the $N(^4S^o_{3/2})$ conservation
$m_e, m_{X_i}, \ldots$	=	particle mass, kg
n	=	numbers of the elementary processes involved in the electron conservation
n_e	=	electron density, m^{-3}
p	=	pressure in downstream flow (where x is greater than 0), Pa
p_0	=	pressure in upstream flow (where x is less than 0), Pa
Q_R	=	radiative losses, $W \cdot m^{-3}$
R	=	characteristic length scale of the flow, m
r_e	=	equilibrium distance of the excited state potential curve, m
T_A	=	heavy particle temperature in downstream flow (where x is greater than 0), K
T_{A0}	=	heavy particle temperature in upstream flow (where x is less than 0), K
T_e	=	electron temperature, K
T_{exc}	=	electronic excitation temperature, K
$T_{v,i}$	=	vibrational temperature of the group of molecules number i, K
t	=	elapsed time from the launch for the FIRE II experiment, s
u	=	velocity in downstream flow (where x is greater than 0), $m \cdot s^{-1}$
u_0	=	velocity in upstream flow (where x is less than 0), velocity of the Flight Investigation of Reentry Environment II probe, $m \cdot s^{-1}$
v	=	vibrational quantum number of the ground electronic state $X^1\Sigma_g^+$ of N_2
$v_{\max}$	=	maximum value of v
v_{X_i}	=	diffusion velocity of X_i, $m \cdot s^{-1}$
X	=	chemical species
x	=	position in downstream flow, m
$x_{\min}$, $x_{\max}$	=	nondimensional characteristic energy
y	=	mass fraction
z	=	altitude of the Flight Investigation of Reentry Environment II probe, m
α	=	power of T of the preexponential factor in the modified Arrhenius law

*Centre National de la Recherche Scientifique, Campus Universitaire du Madrillet; CORIA/UMR 6614/Normandie Université/Centre National d'Etudes Spatiales; Julien.Annaloro@cnes.fr.

†Associate Professor, Centre National de la Recherche Scientifique, Campus Universitaire du Madrillet, CORIA/UMR 6614/Normandie Université; Arnaud.Bultel@coria.fr. Senior Member AIAA.

‡Avenue Edouard Belin; Pierre.Omaly@cnes.fr.

ΔE	=	excitation threshold, eV
ϵ	=	electron energy, eV
$\epsilon_{\max}$	=	characteristic energy, eV
Λ_{ji}	=	escape factor for the radiative transition $j \rightarrow i$
λ	=	wavelength, nm
μ	=	reduced mass of colliding particles, kg
ρ	=	mass density, $\mathrm{kg} \cdot \mathrm{m}^{-3}$
σ	=	cross section, m^2
Ω_{Ae}	=	source term resulting from heavy particle–electron collisions, $\mathrm{W} \cdot \mathrm{m}^{-3}$
ω_e	=	first vibrational spectroscopic constant, eV
$\dot{\omega}_{X_i}$	=	collisional and radiative number density source term for X_i, $\mathrm{m}^{-3} \cdot \mathrm{s}^{-1}$
$\dot{\omega}^+$, $\dot{\omega}^-$	=	positive and negative contributions, respectively, to $\dot{\omega}$

I. Introduction

THE formation of the plasma produced during the entry phase of a body into a planetary atmosphere is a complex process [1]. Indeed, the incident gas to the body's surface undergoes a sudden deceleration at the wall that leads to the increase in its specific internal energy [2]. This deceleration takes place across a shock front located a few centimeters from the wall and delimits a shock layer. In this layer, the plasma is in thermochemical nonequilibrium with strong gradients, especially in the boundary layer (BL), where the flow releases a part of its energy to the wall owing to the temperature difference between the flow and the surface [3]. The observed heating of the entering body is actually not only due to this transfer. The net energy flux density at the wall corresponds to the concomitant contribution of 1) the convective transfer [4], 2) the absorption of a part of the transmitted radiation produced within the flow [5], and 3) the catalysis phenomena due to the presence of dissociated species recombining at the wall [6]. The common point of these three contributions is found in the central role played by the excited states. They lead to a different internal energy transfer with respect to the equilibrium case. Besides, they are the source of radiation by spontaneous deexcitation. Finally, the energy release to the wall due to catalytic phenomena depends on the excitation of incident and desorbed species from the wall [7]. In this context, the key to the relevant sizing of the thermal protection system (TPS) of the entering body requires a detailed knowledge of the behavior of the excited species, not only in the flow but also at the wall.

Since the beginning of the last decade, numerous experimental and modeling studies have been performed to bring into light the behavior of the excited species in typical planetary atmospheric entry plasmas. As far as the modeling studies are concerned, two approaches are used.

The first approach (approach 1) consists of considering the classical global chemical mechanisms, the most known of which are undoubtedly due to Park et al. [8,9]. These mechanisms consist of considering the species as a whole without distinguishing their excited states. Their population number density is then assessed by assuming a Boltzmann distribution at an excitation temperature equal to the electron temperature T_e. The number density can also be assessed by assuming the quasi-steady state, which means that they only depend on the local collisional and radiative elementary processes [10].

The second approach (approach 2) is based on a complete description in the framework of the computational fluid dynamics (CFD), where the particles in their different excited states are considered as full species. A state-to-state approach is then used [11].

Although the strategy of approach 2 for treating the problem is the most relevant one, the strategy of approach 1 remains very useful. Indeed, very high computational resources are needed in the case multidimensional flows are modeled using Navier–Stokes or Euler equations. In addition, treating the excited states as full species requires the knowledge of a very large set of rate coefficients or cross sections for the involved elementary processes. Their availability is sometimes insufficient, and the accuracy of the known data may be inadequate.

However, from the basic point of view, the strategy of approach 1 for treating the problem comes up against several difficulties.

First, the detailed balance principle is fulfilled for elementary processes as the result of microreversibility due to the time-reversal symmetry at the scale of the colliding particles. In contrast, such a "detailed balance" at the scale of the species has no reason to be observed. In other words, the ratio between the dissociation and recombination rate coefficients (considering, globally, the involved species) does not correspond to the equilibrium constant [12]. A similar behavior has been observed in the case of ionization and recombination of carbon, nitrogen, oxygen, and argon atoms for which the ratio between the ionization and recombination rate coefficients departs from the Saha equilibrium constant at high temperature [13]. In this context, treating the chemistry at the scale of the species without a state-to-state approach leads to results, the experimental validation of which can be difficult.

Secondly, the strategy of approach 1 results from the identification of a scenario, which means that a set of processes is considered as playing a role for a specific situation. Although the same species are involved in another situation, the scenario can then be inappropriate in reproducing this new situation. For instance, the CFD treatment of a nitrogen plasma free jet recombining at low pressure using the classical global mechanisms relevant for shock fails in the prediction of the experimental degree of dissociation [14,15]. In addition, using a multitemperature approach fails to model nozzle flows owing to the resulting underestimation of the vibrational distribution tail [16].

Third, the strategy of approach 1 ignores the partial renewal of the elementary cross sections or rate coefficients started at the beginning of the last decade in Europe and the United States [12] because this strategy is based on the use of global rate coefficients identified a long time ago using experimental means. It is important to note that these global rate coefficients were often identified by interpolating experimental profiles of species densities with theoretical ones, taking into account the backward process rate coefficients derived from the forward ones and the equilibrium constant [17–20]. We have underlined previously that this derivation is obviously irrelevant. Whenever possible, modeling has to therefore be performed using a state-to-state approach and benefit from the new database.

From this point of view, nitrogen is a benchmark species for atmospheric entry studies. This is mainly due to its proportion in the Earth's atmosphere. In addition, this molecule is also found in the composition of the atmospheres of Mars and Titan. The interest in nitrogen therefore exceeds the problem of reentries into the atmosphere of Earth and explains why so many experiments and models have been performed so far in order to reveal its behavior. Today, nitrogen is certainly the most referenced case [12]. For one-dimensional flows such as those observed in a shock tube or at the edge of the shock layer along the stagnation streamline in the case of an entering body, a detailed study of the formation of the plasma in nitrogen can therefore be performed by modeling to give valuable information.

Nitrogen was, of course, considered among the species of our former collisional-radiative (CR) model for air (N_2–O_2 mixtures), elaborated on in 2006 [21]. Since that time, this CR model has been implemented in CFD codes modeling shock-induced plasmas using the Rankine–Hugoniot assumptions [22,23] or recombining flows in diverging nozzles [24]. This CR model has been partially validated in compressed flows behind shock waves [25]. This model is electronic state specific and resorts to global dissociation rate coefficients. Vibrationally specific rate coefficients are now available for electron and heavy-particle-induced collisions as well as for other elementary processes for nitrogen (see upcoming sections). A complete updating of the nitrogen model is therefore possible. In addition, this new model can be tested for modeling compressed flows behind a shock front.

The present paper deals with these objectives. The collisional-radiative model for N_2 (CoRaM-N_2) is described. This model is implemented in the conservation equations of a hypersonic flow in thermochemical nonequilibrium using the Rankine–Hugoniot as-

Table 1 Species and states considered in CoRaM-N_2

Species	States
N_2	$X^1\Sigma_g^+(v=0\rightarrow v_{\max}=67)$, $A^3\Sigma_u^+$, $B^3\Pi_g$, $W^3\Delta_u$, $B'^3\Sigma_u^-$, $a'^1\Sigma_u^-$, $a^1\Pi_g$, $w^1\Delta_u$, $G^3\Delta_g$, $C^3\Pi_u$, $E^3\Sigma_g^+$
N_2^+	$X^2\Sigma_g^+$, $A^2\Pi_u$, $B^2\Sigma_u^+$, $a^4\Sigma_u^+$, $D^2\Pi_g$, $C^2\Sigma_u^+$
N	$^4S^o_{3/2}$, $^2D^o = (^2D^o_{5/2} + {}^2D^o_{3/2})$, $^2P^o = (^2P^o_{1/2} + {}^2P^o_{3/2})$, $^4P_{1/2}$, ... (63 states)
N^+	$^3P_0$, $^3P_1$, $^3P_2$, $^1D_2$, $^1S_0$, $^5S^o_2$, $^3D^o_3$, $^3D^o_2$, $^3D^o_1$
e^-	— —

sumptions. This CR model takes into account N_2, N_2^+, N, N^+, and free electrons. The model is vibrationally specific for the N_2 molecules on their electronic ground state and electronically specific for all species. Thus, it is possible to simulate realistically the phase of ladder-climbing vibrational excitation, the resulting dissociation, and the subsequent phase of ionization. Radiative elementary processes are accounted for by using the concept of an escape factor, which allows the treatment of partially optically thick plasmas.

The paper first presents the model used and the cross sections and/or rate coefficients adopted to describe the elementary processes between excited states. Then, a first test-case related to the Flight Investigation of Reentry Environment (FIRE) II probe at medium altitude is treated. A detailed analysis of the global dissociation and ionization of the plasma is performed. A second case is treated relative to higher altitude for which the relaxation takes place over a larger region.

II. Physical Modeling

A. Species and Energy Diagram

As far as the electronic ground state $X^1\Sigma_g^+$ of N_2 is concerned, the model developed in this paper is vibrationally specific. The model takes into account each of the 68 vibrational states ($0 \le v \le v_{\max} = 67$) pointed out by Armenise et al. [26]. The excited electronic states of N_2 are also taken into account without distinguishing the vibrational states. The highest excited electronic state is the $E^3\Sigma_g^+$ state, the excitation energy of which is higher than 11.5 eV from the ground state. Electronic excited states of N_2^+ are also accounted for. The highest excited state is the $C^2\Sigma_u^+$ state, which corresponds to an excitation energy higher than 8 eV. N atoms and N^+ ions are also taken into account. Their characteristics are taken from the National Institute of Standards and Technology (NIST) database.[§] The states of N have been, in part, lumped together. Thus, a set of 63 states has been derived from the NIST database. The energy of the highest excited state is 14.460 eV. For N^+, only the first nine states of the NIST database have been used. The energy of the highest excited state is 11.512 eV from the ground state. The energy diagram of the species is enlarged with respect to the one of the former model elaborated on in 2006 [21].

Table 1 lists the 156 states considered for N_2, N_2^+, N, and N^+.

B. Collisional-Radiative Model

1. *Collisional Elementary Processes*

The different species collide with heavy particles (temperature T_A) and electrons (temperature T_e). $N_2(X, v)$ can be vibrationally excited under electron collisions vibrational process under electron impact (Ve processes) or N_2 or N collisions vibration-translation process under molecular impact (VT-m processes) and vibration-translation process under atomic impact (VT-a processes), respectively. As far as the electron-induced collisions are concerned, the rate coefficients have been calculated by Laporta et al. [27] and can be freely downloaded from the Phys4Entry project database Web site.[¶] The rate coefficients for the vibrational excitation due to heavy particle collisions have been calculated by Armenise et al. [28] and Esposito et al. [29]. Their data have been used.

For the dissociation of N_2 under N_2 dissociation by vibration-translation process under molecular impact (DVT-m processes) or N dissociation by vibration-translation process under atomic impact (DVT-a processes) collisions, the data of Armenise et al. [28] and Esposito et al. [29] have also been used. In contrast, no rate coefficient is available for the processes $N_2(X, v) + e^- \rightarrow 2N(^4S^o_{3/2}) + e^-$ dissociation by vibrational excitation under electron impact (DVe processes) and predissociation. We have assumed that the dissociation occurs when a hypothetical superexcited vibrational state $N_2(X, v = 68)$ is populated. Since the energy difference between the last high-lying state $N_2(X, v = 67)$ and the continuum is negligibly small, we have considered that the rate coefficient is the same as the one related to the excitation of $N_2(X, v = 67)$. Therefore, the rate coefficients of Laporta et al. [27] have been used.

In the literature, many rate coefficients involving the electronic ground state $X^1\Sigma_g^+$ of N_2 are available [30]. These rate coefficients are usually expressed under the well-known modified Arrhenius form

$$k(T) = AT^{\alpha}\exp\left(-\frac{B}{T}\right) \tag{1}$$

Unfortunately, they are often given for the entire electronic state without distinguishing the vibrational states. Since the CoRaM-N_2 does not resort to any assumption about the vibrational distribution of the $X^1\Sigma_g^+$ state of N_2, the vibrational state-dependent rate coefficient has to be assessed. Such rate coefficients are in part available in the literature. Indeed, Capitelli and Celiberto [31], Capitelli et al. [32], and Kosarim et al. [33] put forward vibrationally resolved cross sections for global dissociation and ionization of $N_2(X)$ molecules. State-resolved excitation cross sections have also been calculated. Unfortunately, all the excited states reported in Table 1 are not considered. In addition, a part of these data concerns the lower vibrational states ($v \le 40$). Moreover, separating the contribution of the different channels of reaction has to be performed: for example, in the case of dissociation, since a total rate coefficient is given. Despite these relevant data, we prefer to estimate directly the state-dependent rate coefficient from the total rate coefficient. This is performed using a vibrational reallocation procedure (VRP) of the rate coefficient. This procedure consists of assuming that the previous total rate coefficient is linked to the individual rate coefficient $k_v(T)$ by the summation [26,34]

$$k(T) \equiv k_{\Sigma_v}(T) = \sum_v \frac{[N_2(X, v)]}{[N_2(X)]} k_v(T) \tag{2}$$

Since the total rate coefficient is given as a function of T, we state that the vibrational distribution is of the Boltzmann type for the calculation of the different k_v, which leads to the identification of their parameters A, α, and B assuming they also respect the form [Eq. (1)]. In Table 2, the indication of VRP means that this procedure has been used. Additional details can be found in [35].

The dissociation phenomena starting from the electronically excited states of N_2 are taken into account under electron impact. We have used the rate coefficients calculated by Teulet et al. for the electron-induced collisions [36]. The rate coefficients of the electron-induced dissociation of N_2^+ are also due to Teulet et al. In case the rate coefficient refers to excited states not reported in [36], we have assumed that this rate coefficient is

$$k(T_e) = A\left(\frac{r_e}{a_0}\right)^2 \frac{E_d}{E_d(X)} T_e^{-0.5}\exp\left(-\frac{E_d}{k_B T_e}\right) \tag{3}$$

where a_0 is the first Bohr radius and $A = 6.17 \times 10^{-12}$ $m^3 \cdot s^{-1} \cdot K^{0.5}$, assuming a dissociation cross section of the form [37]

[§]Data available online at http://www.nist.gov/pml/data/asd.cfm [retrieved 2014].

[¶]Data available online at http://phys4entrydb.ba.imip.cnr.it/Phys4EntryDB/ [retrieved 2014].

Table 2 Elementary processes of CoRaM-N_2 with specific procedure (cf. Sec. II.B.1 and Table 3)

Elementary process	Parameters of the rate coefficient k of Eq. (1), $m^3 \cdot s^{-1}$			Reference
	A	α	B	
$N_2(X^1\Sigma_g^+) + e^- \rightarrow N_2(A^3\Sigma_u^+) + e^-$	2.233×10^{-18}	0.717	71,493	A, α, and B derived from [30], VRP
$N_2(X^1\Sigma_g^+) + e^- \rightarrow N_2(B^3\Pi_g) + e^-$	3.977×10^{-16}	0.280	85,958	A, α, and B derived from [30], VRP
$N_2(X^1\Sigma_g^+) + e^- \rightarrow N_2(W^3\Delta_u) + e^-$	1.063×10^{-18}	0.843	85,327	A,α and B derived from [30], VRP
$N_2(X^1\Sigma_g^+) + e^- \rightarrow N_2(B'^3\Sigma_u^-) + e^-$	1.430×10^{-17}	0.492	95,079	A, α, and B derived from [30], VRP
$N_2(X^1\Sigma_g^+) + e^- \rightarrow N_2(a'^1\Sigma_u^-) + e^-$	6.802×10^{-19}	0.788	98,471	A, α, and B derived from [30], VRP
$N_2(X^1\Sigma_g^+) + e^- \rightarrow N_2(a^1\Pi_g) + e^-$	2.305×10^{-17}	0.529	99,272	A, α, and B derived from [30], VRP
$N_2(X^1\Sigma_g^+) + e^- \rightarrow N_2(w^1\Delta_u) + e^-$	9.319×10^{-17}	0.330	103,923	A, α, and B derived from [30], VRP
$N_2(X^1\Sigma_g^+) + e^- \rightarrow N_2(G^3\Delta_g) + e^-$	4.960×10^{-14}	−0.119	127,901	A, α, and B derived from [30], VRP
$N_2(X^1\Sigma_g^+) + e^- \rightarrow N_2(C^3\Pi_u) + e^-$	4.413×10^{-14}	−0.111	129,395	A, α, and B derived from [30], VRP
$N_2(X^1\Sigma_g^+) + e^- \rightarrow N_2(E^3\Sigma_g^+) + e^-$	1.562×10^{-20}	0.907	137,419	A, α, and B derived from [30], VRP
$N_2(X^1\Sigma_g^+) + e^- \rightarrow N_2^+(X^2\Sigma_g^+) + 2e^-$	2.750×10^{-19}	1.500	178,027	A, α, and B derived from [30], VRP
$N_2(X^1\Sigma_g^+) + e^- \rightarrow N_2^+(A^2\Pi_u) + 2e^-$	2.953×10^{-18}	0.714	193,623	A, α, and B derived from [30], VRP
$N_2(X^1\Sigma_g^+) + e^- \rightarrow N_2^+(B^2\Sigma_u^+) + 2e^-$	3.817×10^{-19}	0.822	216,810	A, α, and B derived from [30], VRP
$N_2(X^1\Sigma_g^+) + e^- \rightarrow N_2^+(D^2\Pi_g) + 2e^-$	1.888×10^{-18}	0.603	255,026	A, α, and B derived from [30], VRP
$N_2(X^1\Sigma_g^+) + e^- \rightarrow N_2^+(C^2\Sigma_u^+) + 2e^-$	2.200×10^{-18}	0.599	273,610	A, α, and B derived from [30], VRP
$N_2(a'^1\Sigma_u^-) + e^- \rightarrow N(^2D) + N(^2D) + e^-$	2.254×10^{-11}	−0.500	71,166	Eq. (3)
$N_2(a^1\Pi_g) + e^- \rightarrow N(^2D) + N(^2D) + e^-$	2.013×10^{-11}	−0.500	69,426	Eq. (3)
$N_2(w^1\Delta_u) + e^- \rightarrow N(^2D) + N(^2D) + e^-$	2.052×10^{-11}	−0.500	65,470	Eq. (3)
$N_2(G^3\Delta_g) + e^- \rightarrow N(^2S) + N(^2D) + e^-$	7.922×10^{-12}	−0.500	15,683	Eq. (3)
$N_2(E^3\Sigma_g^+) + e^- \rightarrow N(^2S) + N(^2D) + e^-$	7.789×10^{-13}	−0.500	3,202	Eq. (3)
$N_2^+(a^4\Sigma_u^+) + e^- \rightarrow N(^4S) + N^+(^2P) + e^-$	1.743×10^{-11}	−0.500	64,312	Eq. (3)
$N_2^+(D^2\Pi_g) + e^- \rightarrow N(^4S) + N^+(^3P) + e^-$	1.114×10^{-11}	−0.500	26,438	Eq. (3)
$N_2^+(X^2\Sigma_g^+) + e^- \rightarrow N_2^+(a^4\Sigma_u^+) + e^-$	— —	— —	— —	Eq. (6)
$N_2^+(X^2\Sigma_g^+) + e^- \rightarrow N_2^+(D^2\Pi_g) + e^-$	— —	— —	— —	Eq. (6)
$N_2(X^1\Sigma_g^+) + N_2(X^1\Sigma_g^+) \rightarrow N_2(W^3\Delta_u) + N_2(X^1\Sigma_g^+)$	— —	— —	— —	Eq. (7), VRP
$N_2(X^1\Sigma_g^+) + N_2(X^1\Sigma_g^+) \rightarrow N_2(B'^3\Sigma_u^-) + N_2(X^1\Sigma_g^+)$	— —	— —	— —	Eq. (7), VRP
$N_2(X^1\Sigma_g^+) + N_2(X^1\Sigma_g^+) \rightarrow N_2(a'^1\Sigma_u^-) + N_2(X^1\Sigma_g^+)$	— —	— —	— —	Eq. (7), VRP
$N_2(X^1\Sigma_g^+) + N_2(X^1\Sigma_g^+) \rightarrow N_2(a^1\Pi_g) + N_2(X^1\Sigma_g^+)$	— —	— —	— —	Eq. (7), VRP
$N_2(X^1\Sigma_g^+) + N_2(X^1\Sigma_g^+) \rightarrow N_2(w^1\Delta_u) + N_2(X^1\Sigma_g^+)$	— —	— —	— —	Eq. (7), VRP
$N_2(X^1\Sigma_g^+) + N_2(X^1\Sigma_g^+) \rightarrow N_2(G^3\Delta_g) + N_2(X^1\Sigma_g^+)$	— —	— —	— —	Eq. (7), VRP
$N_2(X^1\Sigma_g^+) + N_2(X^1\Sigma_g^+) \rightarrow N_2(C^3\Pi_u) + N_2(X^1\Sigma_g^+)$	— —	— —	— —	Eq. (7), VRP
$N_2(X^1\Sigma_g^+) + N_2(X^1\Sigma_g^+) \rightarrow N_2(E^3\Sigma_g^+) + N_2(X^1\Sigma_g^+)$	— —	— —	— —	Eq. (7), VRP
$N(i) + (N_2 \text{ or } N) \rightarrow N(j) + (N_2 \text{ or } N)$	— —	— —	— —	Eq. (8)
$N^+(i) + (N_2 \text{ or } N) \rightarrow N^+(j) + (N_2 \text{ or } N)$	— —	— —	— —	Eq. (8)
$N(i) + (N_2 \text{ or } N) \rightarrow N^+(j) + (N_2 \text{ or } N) + e^-$	— —	— —	— —	Eq. (8)

$$\sigma(\epsilon) = \pi r_e^2 \left(\frac{\epsilon}{E_d}\right)^{-1} \tag{4}$$

where $\epsilon > E_d$. In Eqs. (3) and (4), E_d refers to the dissociation energy of the state considered, $E_d(X)$ to that of the ground state, ϵ to the electron energy, and r_e to the equilibrium distance of the excited state potential curve.

Electronic excitation can occur under electron impact. For the N_2 molecules, data given in [38] are discussed by Capitelli et al. [30]. These data have been used in our model. In particular, we have interpolated by a modified Arrhenius law [Eq. (1)] the rate coefficients of excitation from the ground state. The related parameters A, α, and B are reproduced in Table 2. For N_2^+, the data due to Teulet et al. [36] have been implemented. When the states involved in the excitation process were not treated in [30,36], we used papers from Brunger and Buckman [39] and Itikawa [40] ($A^3\Sigma_u^+$, $B^3\Pi_g$, $W^3\Delta_u$, $B'^3\Sigma_u^-$, $a'^1\Sigma_u^-$, $a^1\Pi_g$, $w^1\Delta_u$, $C^3\Pi_u$, $E^3\Sigma_g^+$, and $a''^1\Sigma_g^+$ states of N_2) and Ristić et al. ($A^2\Sigma^+$, $B^2\Pi_r$, $B'^2\Delta$, $F^2\Delta$, and $b^4\Sigma^-$ states of NO) [41] in order to identify an analytical form of the excitation rate coefficient. For an optically allowed transition, this rate coefficient is written as

$$k^A(T_e) = \sqrt{\frac{8k_BT_e}{\pi m_e}}\sigma_{\max} b \frac{(b+1)x_{\min} + b + 2}{(b+1)^2} \exp(-x_{\min}) \tag{5}$$

where $\sigma_{\max} = 10^{-20} \exp[-(\Delta E/8.83)^{4.445}]$ m^2 with ΔE (expressed in electron volts) is the excitation threshold, $x_{\min} = \Delta E/(k_BT_e)$, $x_{\max} = \epsilon_{\max}/(k_BT_e)$, $\epsilon_{\max} = 50(\Delta E/10)^{1.812}$ ($\epsilon_{\max}$ and ΔE are expressed in electron volts), and $b = 2.22/(x_{\max} - x_{\min})$. For an optically forbidden transition, the rate coefficient is calculated by

$$k^F(T_e) = \sqrt{\frac{8k_BT_e}{\pi m_e}}\sigma_{\max} \frac{bx_{\min} + 2}{b^3(x_{\max} - x_{\min})} \exp(1 - x_{\min}) \tag{6}$$

with $\sigma_{\max} = 2 \times 10^{-21}$ m^2, $x_{\min} = \Delta E/(k_BT_e)$, $x_{\max} = \epsilon_{\max}/(k_BT_e)$, and $\epsilon_{\max} = 1.12\Delta E + 5$, with $\epsilon_{\max}$ and ΔE expressed in electron volts; and $b = 1 + (x_{\max} - x_{\min})^{-1}$.

For excitation of N or N^+ under electron impact, we have used the rate coefficients calculated in [21] and the well-known cross sections of Drawin [42] integrated over Maxwell–Boltzmann distributions and expressed under analytical forms involving exponential integrals [13,43].

Besides, the rate coefficients related to electronic excitation of N_2, N_2^+, N, and N^+ under N_2 or N impact have been taken from [30,44,45]. When the rate coefficient is not reported in the previous references for N_2 and N_2^+ excitation, we have used an analytical form similar to Eqs. (5) and (6). We have identified this form by analyzing data due to Park et al. [46], Bhadra and Ghosh [47], and Drawin [48]. We have obtained

$$k(T_A) = \sqrt{\frac{8k_BT_A}{\pi\mu}} A \frac{f_{ij}}{\Delta E^2} \frac{2 + x_{\min}}{x_{\min}} \exp(-x_{\min}) \tag{7}$$

with $A = 7.01 \times 10^{-21}$ m$^2 \cdot$ eV^2, ΔE as the excitation threshold (expressed in electron volts), $x_{\min} = \Delta E/(k_BT_A)$, $\mu = m_Am_B/(m_A + m_B)$ as the reduced mass of the colliding particles A and B, and f_{ij} as the mean absorption oscillator strength ($f_{ij} = 10^{-1}$ for an optically allowed transition, and $f_{ij} = 10^{-3}$ for an optically forbidden transition). For N or N^+ excitation under N_2 or N impact, we have interpolated the rate coefficients derived from the cross section put forward by Park [44] and Lotz [45] by

Table 3 Forward collisional elementary processes implemented in CoRaM-N_2

Type	No.	Elementary process: Reacting species	→	Products	Reference
Vibrational processes	1	$N_2(X^1\Sigma_g^+, v) + e^-$	→	$N_2(X^1\Sigma_g^+, w) + e^-$	[27]
	2	$N_2(X^1\Sigma_g^+, v) + e^-$	→	$2N(^4S^o_{3/2}) + e^-$	[27]
	3	$N_2(X^1\Sigma_g^+, v) + (N_2 \text{ or } N)$	→	$N_2(X^1\Sigma_g^+, w) + (N_2 \text{ or } N)$	[28,29]
	4	$N_2(X^1\Sigma_g^+, v) + N(^4S^o_{3/2})$	→	$3N(^4S^o_{3/2})$	[29]
	5	$N_2(X^1\Sigma_g^+, v_{max}) + N_2$	→	$2N(^4S^o_{3/2}) + N_2$	[28]
	6	$N_2(X^1\Sigma_g^+, v_1) + N_2(X, v_2)$	→	$N_2(X^1\Sigma_g^+, w_1) + N_2(X, w_2)$	[28]
	7	$N_2(X^1\Sigma_g^+, v_{max}) + N_2(X, v)$	→	$2N(^4S^o_{3/2}) + N_2(X^1\Sigma_g^+, v-1)$	[28]
Dissociation	8	$N_2(i \neq X) + e^-$	→	$N(j) + N(k) + e^-$	[36]
	9	$N_2^+(i) + e^-$	→	$N(j) + N^+(k) + e^-$	[36]
Electronic excitation	10	$N_2(i) + e^-$	→	$N_2(j) + e^-$	[30]
	11	$N_2(i) + (N_2 \text{ or } N)$	→	$N_2(j) + (N_2 \text{ or } N)$	[30,50]
	12	$N_2^+(i) + e^-$	→	$N_2^+(j) + e^-$	[36]
	13	$N(i) + e^-$	→	$N(j) + e^-$	[21,42]
	14	$N(i) + N_2$	→	$N(j) + N_2$	[30,44,45]
	15	$N(i) + N$	→	$N(j) + N$	[30,44,45]
	16	$N^+(i) + e^-$	→	$N^+(j) + e^-$	[42]
	17	$N^+(i) + (N_2 \text{ or } N)$	→	$N^+(j) + (N_2 \text{ or } N)$	[44,45]
Excitation transfer	18	$N_2(A) + N_2(A)$	→	$N_2(X^1\Sigma_g^+) + N_2(B)$	[30]
	19	$N_2(A) + N_2(A)$	→	$N_2(X^1\Sigma_g^+) + N_2(C)$	[50]
	20	$N_2(A) + N_2(B)$	→	$N_2(X^1\Sigma_g^+) + N_2(C)$	[49]
	21	$N_2(A) + N(^4S^o_{3/2})$	→	$N_2(X^1\Sigma_g^+) + N(^2P^o)$	[30]
	22	$N_2(B) + N(^4S^o_{3/2})$	→	$N_2(X^1\Sigma_g^+) + N(^2P^o)$	[49]
	23	$N_2(C) + N(^4S^o_{3/2})$	→	$N_2(X^1\Sigma_g^+) + N(^2P^o)$	[49]
Ionization	24	$N_2(i) + e^-$	→	$N_2^+(j) + 2e^-$	[30,36]
	25	$N(i) + e^-$	→	$N^+(j) + 2e^-$	[21,42,51]
	26	$N(i) + N_2$	→	$N^+(j) + e^- + N_2$	[44,45]
	27	$N(i) + N$	→	$N^+(j) + e^- + N$	[44,45]
Charge exchange	28	$N_2(X^1\Sigma_g^+) + N^+(^3P_0)$	→	$N_2^+(X) + N(^4S^o_{3/2})$	[50]
	29	$N_2(X^1\Sigma_g^+) + N^+(^3P_0)$	→	$N_2^+(A) + N(^4S^o_{3/2})$	[50]
Dissociative recombination	30	$N_2^+(X) + e^-$	→	$N(^4S^o_{3/2}) + N(^2D^o \text{ or } ^2P^o)$	[52]
	31	$N_2^+(X) + e^-$	→	$N(^2D^o) + N(^2D^o)$	[52]

$$k(T_A) = \sqrt{\frac{8k_B T_A}{\pi\mu}}\sigma_0 a_1 x_{\min}^{a_2} \exp(-x_{\min}) \tag{8}$$

with $\sigma_0 = 10^{-20}$ m^2, $a_1 = 0.39534$, $a_2 = 0.3546$, and the same notations as in Eq. (7).

Electronic excitation can also result from excitation transfer. Processes involving A, B, and C states of N_2 have been taken into account. They are mainly due to collisions with N_2 molecules and N atoms on their ground and metastable states. The rate coefficients used are taken from [30,49,50].

N_2^+ and N^+ ions can be formed under electron or heavy particle impact of N_2 and N. For electronic ground and excited states of N_2 leading to ionization under electron impact, the data calculated by Teulet et al. [36] and those collected by Capitelli [30] and Uyrova and Ivanov [38] have been used. For electrons ionizing electronic ground ($^4S^o_{3/2}$) and metastable ($^2D^o$ and $^2P^o$) states of N, we have used the data of Kim and Desclaux [51] interpolated under the form of Eq. (1) [21]. For the other states, the cross sections of Drawin [42] and the data already discussed in [21] have been used. Ionization under heavy particle impact has been little studied. We have used the rate coefficient of Eq. (8) derived from the cross sections assumed by Park [44] in relation with the work of Lotz [45].

Charge-exchange processes also take place. The related rate coefficients are deduced from the work of Kossyi et al. [50]. The concerned molecular ions can recombine dissociatively by forming either an electronic ground state or metastable states of N, the rate coefficients and the branching ratios of which have been experimentally determined by Peterson et al. [52].

The previous set of forward collisional elementary processes is listed in Table 3. The rate coefficients having received a specific treatment are listed in Table 2. The backward collisional elementary processes are also implemented in CoRaM-N_2, and each related rate coefficient is derived from the forward rate coefficient and the corresponding equilibrium constant (computed analytically over the [200 K; 65,000 K] range) using the detailed balance principle. Thus, the previous set represents a total of about 40,000 forward and backward elementary processes, and further details are given in [35].

2. *Radiative Elementary Processes*

The species considered in CoRaM-N_2 can deexcite through spontaneous emission. For N_2, the first and second positive systems ($B^3\Pi_g \rightarrow A^3\Sigma_u^+$ and $C^3\Pi_u \rightarrow B^3\Pi_g$ transitions, respectively) have been implemented by using the Einstein coefficients A_{ji} due to Chauveau [53]. This work has also been used for Einstein coefficients related to the first negative system of N_2^+ ($B^2\Sigma_u^+ \rightarrow X^2\Sigma_g^+$ transition). For N, the NIST database has provided the required Einstein coefficients. The lumping procedure used to reduce the number of excited states finally leads to a total of 112 different transitions for N and N^+.

Radiation resulting from the previous transitions can be self-absorbed. This effect is taken into account using the concept of escape factor Λ_{ji} [54]. We have assumed that the broadening of the line at the wavelength λ is only due to the Doppler effect resulting from the relative motion of particles during spontaneous emission. As a result, each escape factor is calculated from [21]

$$\Lambda_{ji} = \int_0^1 \frac{\exp[-\sqrt{m_{X_j}/2\pi k_B T_A}(\lambda^3 A_{ji}/8\pi)(1 - ([X_j]/[X_i])(g_i/g_j))[X_i](g_j/g_i)R\zeta]\,\mathrm{d}\zeta}{\sqrt{-\pi \ln \zeta}} \tag{9}$$

Table 4 Radiative elementary processes implemented in CoRaM-N_2

System	Process no.	Transition: Upper state	→	Lower state	Reference
First positive	32	$N_2(B^3\Pi_g)$	→	$N_2(A^3\Sigma_u^+) + h\nu$	[53]
Second positive	33	$N_2(C^3\Pi_u)$	→	$N_2(B^3\Pi_g) + h\nu$	[53]
Third negative	34	$N_2^+(B^2\Sigma_u^+)$	→	$N_2^+(X^2\Sigma_g^+) + h\nu$	[53]
Atomic spontaneous emission	35	$N(i)$	→	$N(j < i) + h\nu$	NIST
Ionic spontaneous emission	36	$N^+(i)$	→	$N^+(j < i) + h\nu$	NIST

which therefore depends on T_A. Λ_{ji} also depends on the population number density of the upper j and lower i states of the transition, and on the related Einstein coefficient. The flow characteristic length scale, denoted as R, also plays a role in the magnitude of the escape factor. Indeed, Λ_{ji} tends to 1 or to 0 if R tends to 0 or to $+\infty$, respectively. A value of $R = 5 \times 10^{-2}$ m has been chosen as representative of the typical thickness of the shock layer and of the radius of shock tubes in which shock wave propagation experiments are performed. Table 4 summarizes the different radiative transitions implemented in CoRaM-N_2.

C. Conservation Equations

As mentioned in the Introduction (Sec. I), the formation of the shock layer in front of the entering body results from the conversion

$$\text{kinetic energy} \rightarrow \text{internal energy}$$

owing to the sudden deceleration of the flow. In addition to specific activities leading to study this conversion in situ using probes like FIRE II [55], for instance, shock tubes facilities have been extensively used to characterize the plasma formation just behind the shock front. In this context, our CoRaM-N_2 has therefore been implemented in species, momentum, and energy conservation equations in order to be specifically applied to these one-dimensional situations.

The plasma is in thermal and chemical nonequilibrium. Each species X on its excited state i has a mass fraction defined as

$$y_{X_i} = \frac{\rho_{X_i}}{\rho} \tag{10}$$

where ρ_{X_i} is the mass density of X_i in the mixture, the mass density of which is ρ. The flow conditions considered here can be treated by the aerodynamic (Navier–Stokes) equations, since the related Knudsen number does not exceed 0.05 (see [56]). Capitelli et al. [30] indicate that this approach is relevant for vehicle entries at altitudes lower than 100 km. The general conservation equation of X_i is written under the form

$$\frac{\partial \rho_{X_i}}{\partial t} + \frac{\partial}{\partial x_j}(\rho_{X_i} u_j + \rho_{X_i} v_{X_i j}) = m_{X_i} \dot{\omega}_{X_i} \tag{11}$$

with u_j as the gas velocity, $v_{X_i j}$ as the diffusion velocity of X_i, m_{X_i} as the mass of X_i, and $\dot{\omega}_{X_i}$ as the number of X_i particles formed per unit volume and per unit time. The mass source term $m_{X_i}\dot{\omega}_{X_i}$ results from the collisional and radiative elementary processes described in Secs. II.B.1 and II.B.2. In the present context, the characteristic timescales for the expansion or the contraction of the flow τ_{ec} and for diffusion τ_d are much longer than the convective timescale τ_c [37]. In the upcoming sections, we focus our attention on the steady propagation of the flow along the x-axis direction. Introducing the mass fraction y_{X_i}, general conservation equation (11) is therefore reduced to

$$\frac{\mathrm{d}y_{X_i}}{\mathrm{d}x} = \frac{m_{X_i}\dot{\omega}_{X_i}}{\rho u} \tag{12}$$

The cross-section area of the flow is uniform in the case of a shock tube. This cross-section area can also be considered as uniform in a first approximation for the flow behind the shock front along the stagnation streamline in the case of a shock layer. As a result, the momentum conservation equation takes the simple form

$$\frac{\mathrm{d}}{\mathrm{d}x}(p + \rho u^2) = 0 \tag{13}$$

where p is the pressure. The pressure of the flow remains low. The Dalton's law is therefore fulfilled [57]. The pressure p is given by the summation $p = p_A + p_e$, where

$$p_A = \rho k_B T_A \sum_{j \in \mathcal{H}} \frac{y_j}{m_j} \tag{14}$$

is the contribution of the heavy particles ($\mathcal{H}$ stands for the set of indices of the heavy particles) and where

$$p_e = \rho k_B T_e \frac{y_e}{m_e} \tag{15}$$

is the electron pressure. The mass of a heavy particle is m_j, and m_e is the electron mass.

Temperatures T_A and T_e involved in Eqs. (14) and (15) play a major role in the energy conservation equations for heavy species

$$\frac{\mathrm{d}}{\mathrm{d}x}\left[u\left(e_A + p_A + \rho_A \frac{u^2}{2}\right)\right] = \Omega_{Ae} - Q_R \tag{16}$$

and electrons

$$\frac{\mathrm{d}}{\mathrm{d}x}\left[u\left(e_e + p_e + \rho_e \frac{u^2}{2}\right)\right] = -\Omega_{Ae} \tag{17}$$

where

$$\rho_A = \rho \sum_{j \in \mathcal{H}} y_j$$

and $\rho_e = \rho y_e$. In Eqs. (16) and (17), Ω_{Ae} is the energy exchanged per unit volume and per unit time within the flow between heavy particles and electrons owing to the elastic and inelastic (processes with threshold leading to the increase in the excitation energy of the collision partners)/superelastic (processes without threshold, leading to the conversion of excitation energy into kinetic energy) collisions. Q_R is the energy lost by the flow per unit volume and per unit time through radiation. These source terms depend on the collisional and radiative elementary processes described in the previous sections. The internal energy per unit volume for heavy particles and electrons are e_A and e_e, respectively. Variable e_e is reduced to the translational contribution

$$e_e = \frac{3}{2}\rho k_B \frac{y_e}{m_e} T_e \tag{18}$$

Conservation equations (12) and (17) include the influence of the secondary electrons on e_e. The internal energy per unit volume for heavy particles is $e_A = e_A^T + e_A^R + e_A^V + e_A^E$ with the translational contribution

$$e_A^T = \frac{3}{2}\rho k_B \sum_{j\in\mathcal{H}} \frac{y_j}{m_j} T_A \tag{19}$$

The rotational contribution is calculated by assuming the rotational mode is well coupled with the translational mode of heavy species

$$e_A^R = \rho k_B \sum_{j\in\mathcal{R}} \frac{y_j}{m_j} T_A \tag{20}$$

where $\mathcal{R}$ stands for the set of indices of the molecules. The vibrational contribution results from the vibrational states of $N_2(X)$ and from the other electronic states of N_2 and N_2^+. The latter are assumed to be populated following a Boltzmann distribution at T_e so that

$$e_A^V = \rho\left[\sum_v \frac{y_{N_2,v}}{m_{N_2}} E_v + \sum_{j\in\mathcal{S}} \left(\frac{1}{2} + \frac{1}{\exp(\omega_{e,j}/k_B T_e) - 1}\right) \frac{y_j}{m_j} \omega_{e,j}\right] \tag{21}$$

where $\mathcal{S}$ stands for the set of indices of all the molecular states except $N_2(X)$. E_v and $\omega_{e,j}$ refer to the energy of a vibrational state of $N_2(X)$ and to the first vibrational spectroscopic constant (harmonic oscillator quantum energy) of the electronic excited state j, respectively. The electronic contribution is

$$e_A^E = \rho \sum_{j\in\mathcal{S}\cup\mathcal{A}} \frac{y_j}{m_j} E_j \tag{22}$$

for which the formation enthalpy of the excited state j is taken into account in the value of E_j. $\mathcal{A}$ stands for the set of indices of the electronic states of N and N^+.

Solving the problem requires one to solve 160 conservation equations. One equation is for electrons, 156 are for the atomic and molecular states, and three equations are for u, T_A, and T_e resulting from Eqs. (13), (16), and (17). The resulting set of ordinary differential equations is solved using the DVODE library [58], which is the more efficient solver for highly stiff problems [59].

III. Application to Hypersonic Flows

A. Medium Mach Number Conditions: $\mathscr{M}_0 \approx 30$

The first studied test case corresponds to a Mach number close to 30 at medium pressure. These conditions were those of the FIRE II probe near the peak heating undergone by the thermal protection system [55]. Precisely, we have chosen the elapsed time $t = 1642.5$ s from the launch for which the probe flew at a low altitude (LA) of $z = 54$ km. The day of this flight, a Nike–Apache sounding rocket was launched in order to measure as accurately as possible the atmospheric pressure and temperature conditions along the FIRE II probe trajectory. The results depart slightly from the U.S. standard atmosphere [60] for the pressure for $z > 45$ km and for the temperature over the ranges 25 km $< z <$ 54 km and $z > 76$ km. We have therefore adopted as the LA atmospheric conditions those related to the Nike–Apache rocket results ($p_0 = 54$ Pa and $T_{A0} = 274$ K), which leads to a probe Mach number of $\mathscr{M}_0 = 32.0$. The present test case is summarized in Table 5.

The shock front is assumed to be a discontinuity across which the upstream conditions $\mathscr{M}_0 = 32.0$, $p_0 = 54$ Pa, and $T_{A0} = 274$ K suddenly jump to the downstream conditions $\mathscr{M}(0)$, $p(0)$, and $T_A(0)$. The jump conditions are driven by the Rankine–Hugoniot equations [61] based on mass, momentum, and energy conservations, assuming that the rotational mode is immediately coupled with the translational mode, whereas the electronic and vibrational modes are frozen [37]. At $x = 0$, the temperature of heavy particles T_A is then much higher than T_{A0}. In contrast, the electron temperature T_e is equal to that of the upstream flow because the electron gas sound speed strongly exceeds the incident gas velocity. In other words, the flow is electronically subsonic [62] and electrons are not perturbed by the shock front. The forward processes of Tables 2 and 3 are no longer counterbalanced by the corresponding backward processes, which means that the gas flow is in thermochemical nonequilibrium. Therefore, the gas composition spatially evolves downstream (for $x > 0$) in order to asymptotically recover the local thermodynamic equilibrium (LTE).

Table 5 FIRE II probe flight characteristics and related upstream conditions for shock tube hypersonic flows

	FIRE II flight			Atmospheric conditions		
Conditions	z, km	t, s	u_0, km · s^{-1}	p_0, Pa	T_{A0}, K	Mach number $\mathscr{M}_0$
LA	54	1642.5	10.6	54	274	32.0
HA	76	1634.0	11.3	2.2	195	40.4

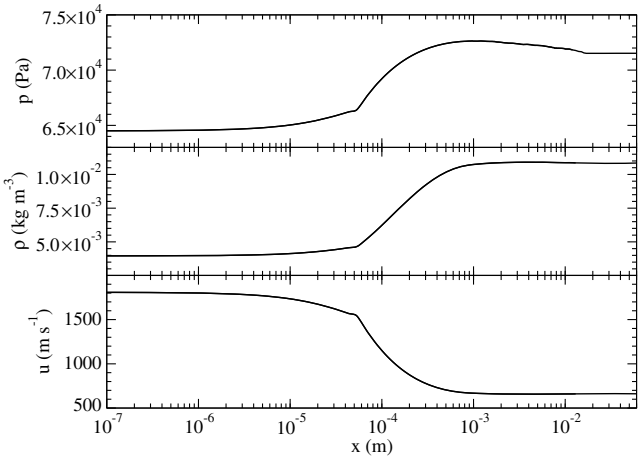

Fig. 1 Postshock spatial evolution of the aerodynamic variables in the medium-Mach-number conditions.

1. *Aerodynamic Variables*

Figure 1 shows the postshock spatial evolution of pressure p, mass density ρ, and velocity u. A logarithmic scale is used for the abscissa instead of a linear scale in order to show the spatial distribution over several orders of magnitude. Indeed, we will see that the whole relaxation typically ranges over three orders of magnitude. Such a logarithmic scale will be systematically used in the upcoming sections. The deceleration of the flow can be observed, since u decreases from $u_0 = 10.6$ km · s^{-1} to $u(0) \approx 1.8$ km · s^{-1}. The pressure increases from $p_0 = 54$ Pa to $p(0) \approx 6.5 \times 10^4$ Pa, and the mass density increases from $\rho_0 = 7 \times 10^{-4}$ kg · m^{-3} to $\rho(0) \approx 4 \times 10^{-3}$ kg · m^{-3}. This illustrates the compression of the flow resulting from the deceleration. It is interesting to note that the profiles present a strong variation around $x = 5 \times 10^{-5}$ m. This is due to the strong variation of the total mass density. Indeed, ρ increases of 10% over 10^{-5} m in order of magnitude. Owing to the coupling with the other aerodynamic variables, notably through Eq. (13), u and p strongly evolve. The strong variation of ρ is discussed in Sec. III.A.3. For $x > 5 \times 10^{-5}$ m, the profiles present lower gradients before a large region where profiles are almost uniform.

2. *Characteristic Temperatures T_A, T_v, T_e, and T_{exc}*

The previous gradients correspond to the region where a strong decrease in T_A is observed, as shown by Fig. 2. This decrease is due to the energy pumping resulting from the progressive vibrational excitation of the N_2 molecules. The underlying dynamics is illustrated by the calculation of the vibrational temperature

$$T_{v,i} = -\frac{1}{k_B[(\mathrm{d}/\mathrm{d}E_v)(\ln[\mathrm{N}_2(X,v)])]_{lsl,v_{\min}(i)\to v_{\max}(i)}} \tag{23}$$

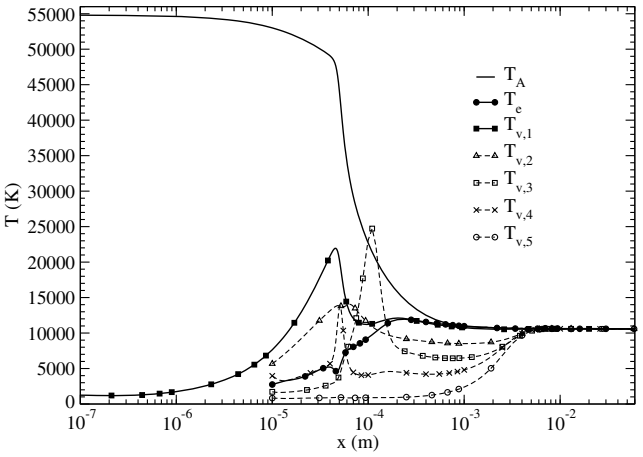

Fig. 2 Same figure as Fig. 1 but for T_A, T_e and the different vibrational temperatures $T_{v,1}$ to $T_{v,5}$ of the electronic ground state $X^1\Sigma_g^+$ of N_2.

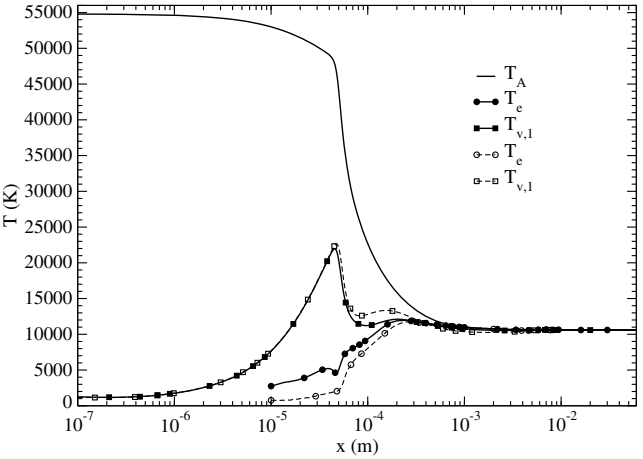

Fig. 3 Same figure as Fig. 2 but without electron-induced collisions leading to vibrational excitation and dissociation (nonfilled symbols).

defined as the excitation temperature of the group number i of vibrational levels corresponding to the vibrational quantum numbers $v_{\min}(i) < v < v_{\max}(i)$. E_v is the vibrational energy (see Sec. II.A) and lsl means that the derivative is the slope of the least-squares line (derived from vibrational distributions and discussed in Sec. III.A.3). Five groups have been defined, such as $0 \le v \le 19$ for $i = 1$, $20 \le v \le 39$ for $i = 2$, $40 \le v \le 49$ for $i = 3$, $50 \le v \le 59$ for $i = 4$, and $60 \le v \le 67$ for $i = 5$. Thus, the first group is representative of the vibrational energy storage, the conservation of which is modeled by a specific equation when no vibrationally specific approach is used [63]. Since the vibrational levels have a population number density negligibly small in the upstream flow for $v > 0$, the vibrational temperatures $T_{v,2}$ to $T_{v,5}$ are displayed in Fig. 2 only for $x > 10^{-5}$ m. Figure 2 shows that the increase in $T_{v,i}$ is delayed according to the value of i. We can see the influence of the vibrational excitation of the ladder-climbing-type resulting from the initial ($x = 0$) strong nonequilibrium and the VT-m elementary processes, since electron density and dissociation degree are initially negligibly small. The final coupling with T_A is also delayed and occurs for $x \approx 6 \times 10^{-3}$ m. The dynamics of the vibrational distribution is further analyzed in Sec. III.A.3.

Figure 2 also displays the profile of T_e. Electron temperature progressively increases until a very good coupling, first with the vibrational temperature $T_{v,1}$ for $x \approx 2 \times 10^{-4}$ m, and then with T_A for $x \approx 8 \times 10^{-4}$ m. The coupling with $T_{v,1}$ is the direct result of the Ve elementary process influence, the efficiency in the electron gas heating of which is much higher than elastic collisions. It is interesting to note that, contrary to the flowfield calculated by Colonna et al. [64] in the case of H_2, the influence of elastic collisions is very weak. This is due to the postshock conditions chosen for electron density (mass fraction $y_e = 10^{-17}$), which is much lower than the one chosen by Colonna et al. ($y_e = 5 \times 10^{-14}$). From our point of view, such a value for y_e just behind the shock front is more realistic, since these conditions result from the upstream flow where the temperature is very low and where there are almost no free electrons. We have verified the role of the Ve elementary processes by performing a similar calculation for which the latter processes have been removed. Figure 3 illustrates the obtained profiles. It is interesting to note that the spatial evolution of T_A is not at all modified. In contrast, $T_{v,1}$ is modified after its maximum around $x \approx 4 \times 10^{-5}$ m, where electron density becomes high enough. A part of the available energy remains in the vibrational excitation when the Ve processes are removed; $T_{v,1}$ is then higher, and T_e is weaker. The coupling between $T_{v,1}$ and T_e takes place farther from the shock front for $x \approx 4 \times 10^{-4}$ m. The influence of the Ve elementary processes on the vibrational temperatures $T_{v,2}$ to $T_{v,5}$ is weak, and the related curves have not been plotted in Fig. 3.

To characterize the departure from Boltzmann equilibrium, the excitation temperature

$$T_{\text{exc}}[\text{N}] = -\frac{1}{k_B[(d/dE_j)(\ln([\text{N}(j)]/g(j)))]_{lsl}} \tag{24}$$

is calculated for N atoms for the last 40 excited levels under the ionization limit, and therefore over an energy range of 1 eV. This excitation temperature is defined as the vibrational temperature of Eq. (23). This definition is relevant insofar as excited levels have energies close to each other. There are few electronic excited states for the molecules. Therefore, in contrast with atoms, the excitation temperature based on the least-squares line is irrelevant. The excitation temperature for molecules is based on the population density of the X electronic ground state, such as

$$T_{\text{exc}}[\text{N}_2(i)] = -\frac{E_i - E_X}{k_B \ln\{[Z_r(i)Z_v(i)g_e(i)/Z_r(X)Z_v(X)g_e(X)]([\text{N}_2(X)]/[\text{N}_2(i)])\}} \tag{25}$$

where Z_r, Z_v, and g_e are the rotational and vibrational partition functions, and the electronic statistical weight, respectively. The rotational partition function is calculated using the rigid rotor approximation with T_A. The vibrational partition function is calculated by directly using the levels considered in the kinetics for $N_2(X)$ and using a development of the second order for the excited states with the first three spectroscopic constants given by Chauveau [53], Huber and Herzberg [65], and Loftus and Krupenie [66]. T_e is used to calculate these vibrational partition functions.

The evolution of $T_{\text{exc}}[\text{N}]$ is displayed in Fig. 4. For $x < 4 \times 10^{-5}$ m, the excitation temperature is high owing to the influence of the N_2-induced collisions. Then, for 4×10^{-5} m $< x < 3 \times 10^{-4}$ m, we can observe that $T_{\text{exc}}[\text{N}]$ undergoes a strong decrease before a coupling with T_e (see Fig. 2) for $x \approx 4 \times 10^{-4}$ m. This decrease is due to the pumping of the excited states resulting from the global ionization process of the flow. This effect has been already noted in various situations, notably in the framework of our determination of the global ionization rate coefficients of N under electron impact [13,37]. The final coupling means that excitation equilibrium is reached for N atoms under electron impact.

Figure 4 also shows the spatial profiles of $T_{\text{exc}}[\text{N}_2(i)]$ for the A, B, a, and C states. The excitation temperature for the other states globally presents the same behavior and has not been plotted for clarity. The population densities are frozen with respect to the upstream conditions so that the excitation temperatures are weak for the lowest values of x. Then, collisional excitation takes place, which leads to the increase in the population densities of the A, B, a, and C excited states, whereas $[\text{N}_2(X)]$ decreases owing to the dissociation. The excitation temperatures increase. In the subsequent part of the evolution (for $x > 8 \times 10^{-5}$ m), they evolve in order to asymptotically reach the other characteristic temperatures of the flow. The

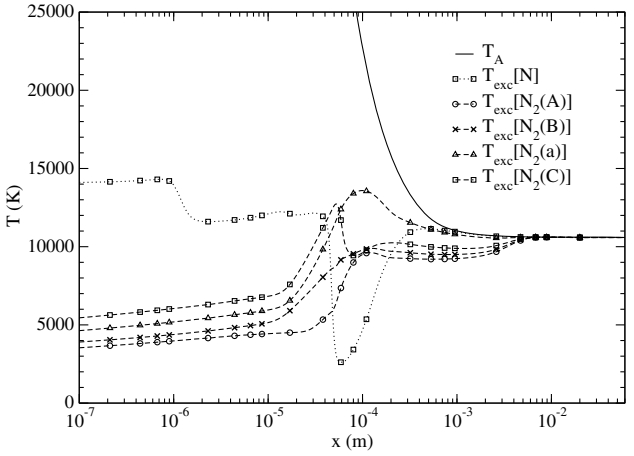

Fig. 4 Same figure as Fig. 2 but for atomic and molecular excitation temperatures defined by Eqs. (24) and (25), respectively.

collisional coupling is reached, and all characteristic temperatures of the flow are equal. This means that the flow is in LTE.

3. Species Number Densities

In the previous section, we have performed an analysis of the behavior of the flow in terms of characteristic temperatures. An easy and detailed assessment of departures from equilibrium has been possible. However, the thorough examination of the behavior of the number densities is necessary. We present first the spatial profiles of the species density in Fig. 5. We can see the dissociation phase for the N_2 molecules. The dissociation degree is $D_d = 10^{-10}$ at $4.8{\times}10^{-6}$ m. The dissociation of the N_2 molecules is a rough phenomenon, since the density of N is multiplied by a factor of 2×10^8 from $x = 10^{-5}$ m to $x = 5 \times 10^{-5}$ m. From $x = 4.5 \times 10^{-5}$ m to $x = 5.5 \times 10^{-5}$ m, the N density is multiplied by a factor of 20, which leads to an increase in ρ of 10%. Then, the coupling between ρ and the other aerodynamic variables leads to the profiles displayed in Fig. 1. Dissociation is immediately followed by ionization. The ionization degree is $D_i = 10^{-10}$ at 1.8×10^{-5} m and increases rapidly over almost the same scale as the dissociation degree. It is interesting to note that the electroneutrality is due to the electrons and the N^+ ions. Indeed, the N_2^+ density is less by a factor greater than 10. For $x > 10^{-2}$ m, the flow composition is quite uniform. Although the flow has reached LTE, weak energy losses may occur by radiation for $x > 10^2$ *m*, which may induce a decrease in the total energy, and therefore in the temperature and in the dissociation degree. In these conditions, the flow would not be at equilibrium, but it would be only characterized by LTE. We observe that the plasma is uniform for $x > 10^{-2}$ m. This is confirmed by

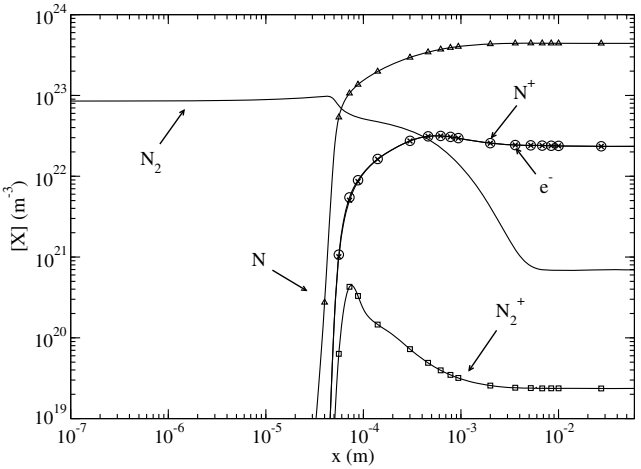

Fig. 5 Spatial profiles of the total number density of N_2, N_2^+, N, N^+, and electrons in the conditions of Fig. 1.

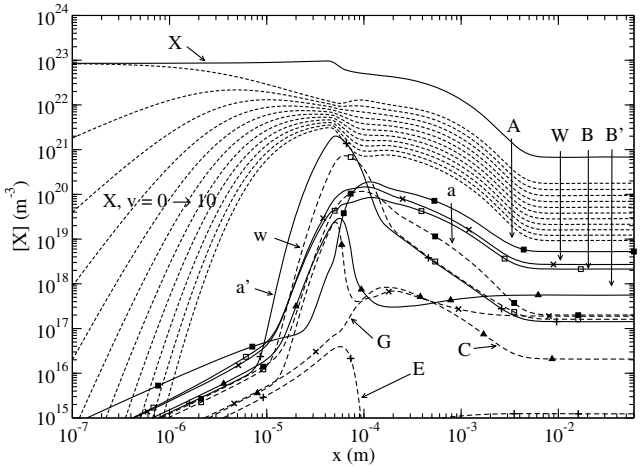

Fig. 6 Same figure as Fig. 5 but for the first 11 vibrational states of $N_2(X)$, the electronic ground state, and the excited states of N_2.

the excitation temperatures profiles. As a result, the plasma is in equilibrium.

The vibrational dynamics illustrates the global dissociation process. Indeed, Fig. 6 displays the spatial profiles of the number density of the first 11 vibrational states of $N_2(X)$. In addition, Fig. 7 shows for different positions the Boltzmann plot of the 68 vibrational states taken into account in CoRaM-N_2. We can see that their number density undergoes a strong increase. The narrowing of the vibrational distribution observed around 4×10^{-5} m on Fig. 6 explains the peak of $T_{v,1}$, previously noted in Fig. 3. The maximum gradient of $[N(^4S^o_{3/2})]$ is obtained for $x_{NG} \approx 5 \times 10^{-5}$ m (cf. discussion in Sec. III.A.5). At this point, the dissociation is the most effective process. The Boltzmann plot is given at the same position on Fig. 7. We see that the last eight vibrational states are strongly underpopulated. They do not follow a Boltzmann distribution at the excitation (vibrational) temperature of the first 11 states. In fact, the dissociation mainly concerns the high-lying vibrational states. This leads to a strong pumping of the involved levels, and therefore to a strong underpopulation with respect to equilibrium. The number density of the first 11 vibrational states is weakly modified by the dissociation. This result underlines the relevance of a vibrational state-to-state modeling of the chemistry within the flow. Since the vibrational temperatures $T_{v,1}$ and $T_{v,5}$ are very different during the dissociation phase, the question of the relevance of the global dissociation rate coefficients depending on T_A and $T_{v,1}$, often used in CFD modelings of this type of flow, is open. The Boltzmann plot obtained for $x = 10^{-2}$ m clearly shows that the vibrational equilibrium is reached since the distribution is linear. We can also note some perturbations in

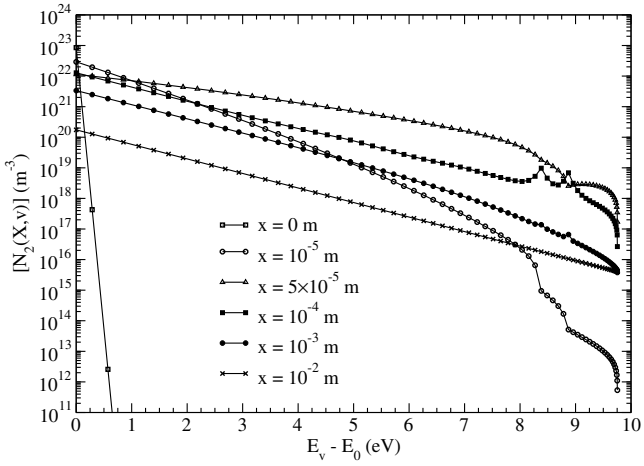

Fig. 7 Boltzmann plot of the $N_2(X)$ vibrational states at different positions in the conditions of Fig. 1. The dissociation limit corresponds to $E_v - E_0 = 9.754$ eV.

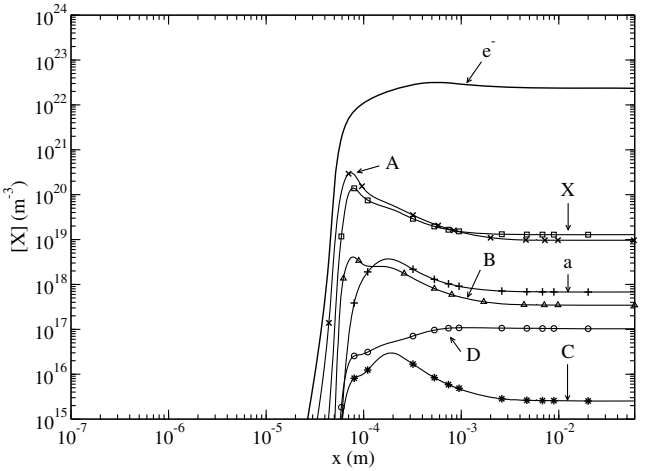

Fig. 8 Same figure as Fig. 6 but for the different states of N_2^+ in the conditions of Fig. 1.

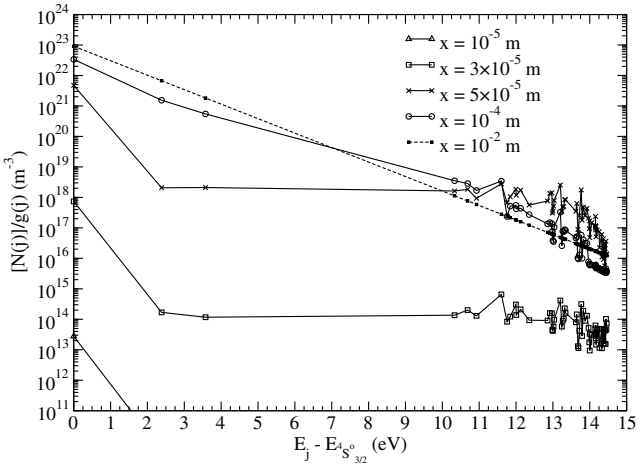

Fig. 10 Boltzmann plot of the N states at different positions in the conditions of Fig. 1. The dissociation limit corresponds to $E_j - E_{^4S^o_{3/2}} = 14.534$ eV.

the Boltzmann distribution for $v = 42$ and $v = 47$. This is due to the energy resonant transfer (energy difference of some 10^{-3} eV) with the a' and w states, respectively. For $x < 5 \times 10^{-5}$ m, the a' and w states limit the increase in the population density of the $v = 42$ and $v = 47$ states, whereas they populate the $v = 42$ and $v = 47$ states for $x < 5 \times 10^{-5}$ m, since their number density is high, as illustrated by Fig. 6. In the case of a discharge in CO, similar effects have been already observed owing to the energy resonant transfer $CO(X, v) + CO \leftrightarrow CO(Y) + CO$ with $(v = 26, Y \equiv a^3\Pi)$ and $(v \simeq 40, Y \equiv A^1\Pi)$ by Farrenq et al. [67].

Figure 6 also illustrates the behavior of the electronic excited states of N_2. Most of them present an increase in their number density due to collisions with heavy particles, followed by a decrease resulting from their dissociation under collisions with heavy particles and electrons. We can note that the B and C states of N_2 are highly populated. They can contribute to radiative losses by the emission of the first and second positive systems (cf. Sec. III.A.4). This can also be the case of the A state of N_2^+ through the first negative system emission. The number density spatial profile of the N_2^+ states is displayed in Fig. 8. In spite of these radiative losses, the flow reaches a final equilibrium.

The dissociation process leads to the increase in the N excited states number density, as illustrated by Fig. 9. The ground and the first two excited (metastable) states are shown. The upper and lower states involved in important radiative transitions are displayed, such as those responsible for the emission of the resonance lines $(N(^4P_{1/2,3/2,5/2}) \rightarrow N(^4S^o_{3/2})$ transitions at $\lambda \approx 120$ nm, [15]), of other vacuum ultraviolet (VUV) lines $(N(^2P) \rightarrow N(^2D^o)$ transitions at 149 nm, $N(^2P) \rightarrow N(^2P^o)$ transitions at 174 nm), and of visible lines $(N(^2D^o_{5/2}) \rightarrow N(^2P_{3/2})$ transitions at 410 nm, $N(^4S^o) \rightarrow N(^4P)$ transitions of the triplet system at 744 nm and $N(^4P^o) \rightarrow N(^4P)$ transitions at 822 nm). The upper states of these transitions are strongly populated and may induce significant radiative losses if the related escape factors are high enough. However, we have seen in Fig. 2 that, once LTE is reached, the different temperature profiles are quite uniform. The plasma is in equilibrium, which means that radiation has a negligible role. The upper state of the $N^+(^3D^o) \rightarrow N^+(^3P)$ resonance transition has a spatial evolution, also plotted in Fig. 9. We can see that, after a strong increase during the ionization phase, the number density relaxes to low values.

Finally, the Boltzmann plot for the N atoms is illustrated by Fig. 10. The behavior is similar to the one already described for the $N_2(X)$ vibrational states. During the ionization phase, a strong depletion of the number density of the levels close to the ionization limit is observed. Subsequently, a linear distribution is obtained. The electronic excitation equilibrium is then reached. The temperature of this Boltzmann distribution is equal to the other characteristic temperatures of the flow, as already noted in Fig. 2.

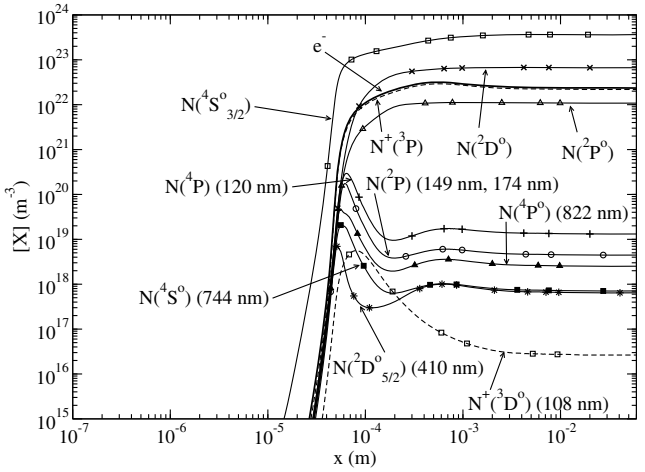

Fig. 9 Same figure as Fig. 6 but for different states of N and N^+ involved in radiative transitions (wavelength indicated between parentheses) in the conditions of Fig. 1.

4. Radiative Aspects

The final equilibrium obtained after relaxation is the result of the predominance of the collisional elementary processes. Despite this equilibrium, the flow radiates, as illustrated by Fig. 11, showing the spatial profiles of some escape factors Λ_{ji}. Indeed, we note that several transitions are almost optically thin, since the related escape factors are close to unity for $x > 2 \times 10^{-3}$ m. It is interesting to note that the B state of N_2 temporary undergoes a population inversion

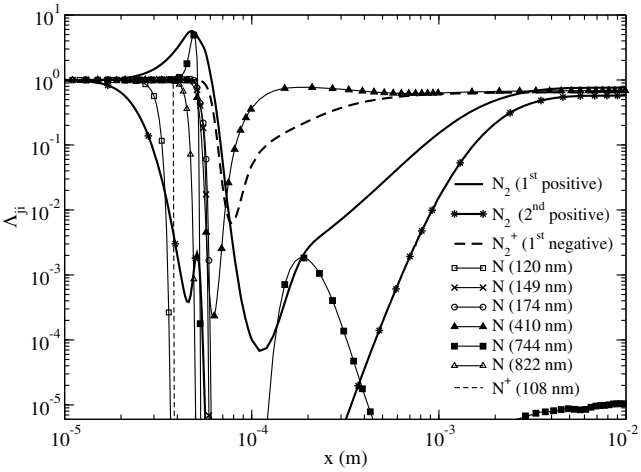

Fig. 11 Spatial profiles of some escape factors.

with respect to the A state, since the escape factor for the first positive system is higher than unity over the region 2×10^{-5} m $< x <$ 6×10^{-5} m. However, these radiative losses taken into account by the source term $-Q_R$ in conservation equation (16) are negligibly small with respect to the other terms. This is directly verified during the calculation. If we add term to term Eqs. (16) and (17), we obtain the total energy conservation equation, the source term of which results from the radiative losses only. The total energy of the flow per unit volume defined as $e_A + e_e + p + \rho\frac{u^2}{2}$ is uniform in the present case, which confirms the negligible role played by radiation.

The negligible role of radiation is confirmed when the radiative elementary processes listed in Table 4 are removed from CoRaM-N_2. The calculation then leads to the same results, even for the upper states of the transitions mentioned in Sec. III.A.3. Radiation definitely has a negligible role on the behavior of the flow.

5. Specific Study of the Populating Processes for $N(^4S^o_{3/2})$ *and Electrons*

A further characterization of the dissociation and ionization phases described in Sec. III.A.3 can be performed by plotting the different contributions of the elementary processes to the positive and negative parts of the gradient of the $N(^4S^o_{3/2})$ and electron densities, respectively. Since the mass fraction of X_i can be expressed as $y_{X_i} = [X_i]m_{X_i}/\rho$, we can derive from species conservation equation (12) the equivalent equation written for the density $[X_i]$ under the form

$$\frac{\mathrm{d}[X_i]}{\mathrm{d}x} = \frac{1}{u}\left(\dot{\omega}_{X_i} - [X_i]\frac{\mathrm{d}u}{\mathrm{d}x}\right) \tag{26}$$

where $\mathrm{d}u/\mathrm{d}x$ is negative (see Fig. 1). Moreover, we can separate the positive (superscript $+$) and negative (superscript $-$) contributions of the elementary processes to $\dot{\omega}_{X_i}$. We have

$$\frac{\mathrm{d}[\mathrm{N}(^4S^o_{3/2})]}{\mathrm{d}x} = \sum_{m\in\mathcal{P}_N}(\dot{\omega}^+_{\mathrm{N}(^4S^o_{3/2}),m} - \dot{\omega}^-_{\mathrm{N}(^4S^o_{3/2}),m}) + \frac{[\mathrm{N}(^4S^o_{3/2})]}{u}\left|\frac{\mathrm{d}u}{\mathrm{d}x}\right| \tag{27}$$

for $N(^4S^o_{3/2})$ and

$$\frac{\mathrm{d}n_e}{\mathrm{d}x} = \sum_{n\in\mathcal{P}_e}(\dot{\omega}^+_{e,n} - \dot{\omega}^-_{e,n}) + \frac{n_e}{u}\left|\frac{\mathrm{d}u}{\mathrm{d}x}\right| \tag{28}$$

for electrons where m and n are the numbers of the concerned elementary processes of Tables 3 and 4. $\mathcal{P}_\mathrm{N}$ and $\mathcal{P}_e$ stand for the set of indices of the elementary processes involving $N(^4S^o_{3/2})$ and electrons, respectively. In each equation, the last term corresponds to the convective contribution.

For $N(^4S^o_{3/2})$, Fig. 12 shows the distribution of the positive and negative contributions of the elementary processes $m \in \mathcal{P}_\mathrm{N} = \{2, 4, 5, 7, 8, 9, 13, 14, 15, 25, 26, 27, 28, 29, 30, 35\}$ (see Tables 3 and 4 for the correspondence between the numbers and the elementary processes). The positive contributions to $\mathrm{d}[\mathrm{N}(^4S^o_{3/2})]/\mathrm{d}x$ are continuous lines, and the negative contributions are dashed lines. Filled symbols, stars, and crosses refer to heavy particle-induced collisions, and nonfilled symbols refer to electron induced collisions. C and black triangles are related to charge-exchange processes, respectively. D and R refer to dissociative recombination and radiative processes, respectively. This figure also shows the distribution of the contribution of the convective term. We see the influence of DVT-m ($m = 5$) and DVT-a ($m = 4$) processes in the dissociation at positions close to the shock front. DVT-a processes are the most efficient processes for the dissociation at $x_{NG} = 5.2\times10^{-5}$ m where the gradient of $[\mathrm{N}(^4S^o_{3/2})]$ is maximum with the value 5.7×10^{27} m^{-4}. Then, the influence of the convective term increases as well as the one of the excitation of N atoms from the ground state under electron ($m = 13$) and N ($m = 15$) collisions. The mixture presents a complex behavior, since dissociative recombination ($m = 30$) and charge exchange ($m = 28$, 29) also play a significant role. It is interesting to note that radiation influences the populating process of $N(^4S^o_{3/2})$ only at positions corresponding to the dissociation of the N_2 molecules. Downstream, radiation ($m = 35$) plays a negligible role, even where the excitation of N atoms is significant. This is due to the collapse of the VUV emission illustrated by Fig. 11 around $x = 5\times10^{-5}$ m. For $x > 10^{-3}$ m, Fig. 12 also shows that each forward elementary process is counterbalanced by the corresponding backward elementary process, which leads to a decrease in $\mathrm{d}[\mathrm{N}(^4S^o_{3/2})]/\mathrm{d}x$. At $x = 6\times10^{-3}$ m, the $N(^4S^o_{3/2})$ number density no longer varies.

Figure 13 displays the contributions to $\mathrm{d}n_e/\mathrm{d}x$. The involved elementary processes refer to $n \in \mathcal{P}_e = \{24, 25, 26, 27, 30, 31\}$. For $x \approx 10^{-5}$ m, the increase in n_e is due to N_2 collisions induced ionization of N atoms ($n = 26$). The maximum gradient (at a value of 2.9×10^{26} m^{-4}) is obtained for $x_{eG} = 6.5\times10^{-5}$ m, whereas the $N(^4S^o_{3/2})$ one is obtained for $x_{NG} = 5.2\times10^{-5}$ m. It is interesting to note that the maximum of the excitation of N_2, N_2^+, and N (see Figs. 6, 8, and 9) is achieved at about the place where the electron and N densities present the strongest gradients. The delay between x_{eG} and x_{NG} underlines the succession of the dissociation and ionization phases. Then, the ionization of N under electron collisions ($n = 25$)

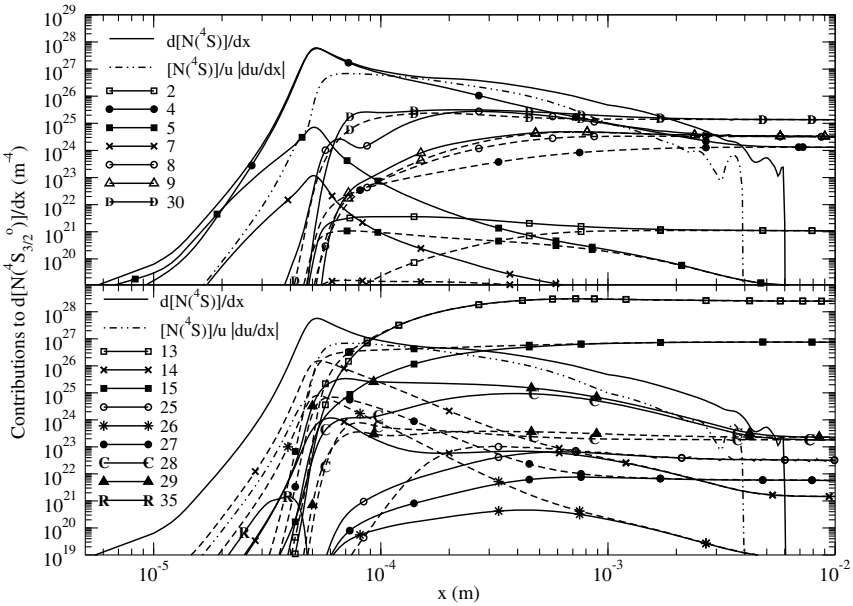

Fig. 12 Contribution to the $N(^4S^o_{3/2})$ populating process.

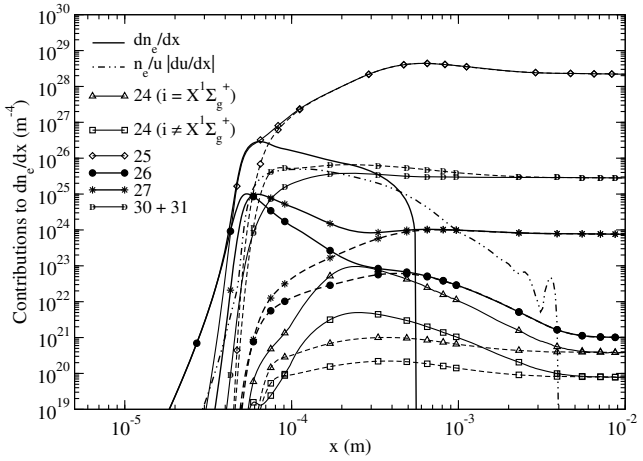

Fig. 13 Same figure as Fig. 12 but for conservation equation (28) for electrons: $n \in \mathcal{P}_e = \{24,25,26,27,30,31\}$ (see Tables 3 and 4).

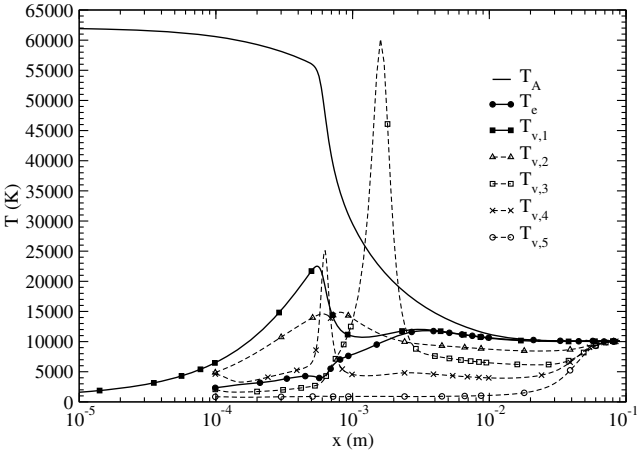

Fig. 14 Same figure as Fig. 2 but for the case of the high-altitude trajectory point of the FIRE II probe (cf. Table 5).

takes over. The convective term plays a role for n_e quite similar to the one observed for $N(^4S^o_{3/2})$. The recombination backward processes of N under electron collisions ($n = 25$) limit the electron density increase, which is mainly driven by the dissociative recombination ($n = 30, 31$) for $x \approx 5 \times 10^{-4}$ m. The direct ionization of $N_2(X^1\Sigma_g^+)$ has a contribution to the global ionization process higher than the electronic excited states, but these two contributions remain negligible with respect to the ionization of N. Finally, we can observe after $x \approx 7 \times 10^{-3}$ m that each forward process is rigorously counterbalanced by its backward process, which means that equilibrium is actually reached.

The latter result is very interesting from the modeling point of view. The typical thickness of the shock layers formed in the LA trajectory conditions is close to $5{\times}10^{-2}$ m. As a result, this value has been chosen for R, which is the characteristic length scale for the calculation of the escape factors Λ_{ji}. In the vicinity of the entering body TPS, the flow heats the wall through a BL. The CFD modeling of this region is performed using Navier–Stokes equations insofar as the flow velocity is small [4]. Separately modeling the BL and the first part of the shock layer is then relevant as long as there is continuity. The boundary-layer edge properties have to coincide with those calculated in the shock layer at the same position from the shock front. For the present LA conditions, we have seen that equilibrium is reached at $x \approx 7 \times 10^{-3}$ m. Since the shock layer thickness is around 5×10^{-2} m, the shock layer is in equilibrium downstream over at least 4×10^{-2} m, and therefore at the edge of the boundary layer.

B. High-Mach-Number Conditions: $\mathscr{M}_0 \approx 40$

Since the radiative losses play a negligible role in the behavior of the flow in the LA conditions, we have chosen to focus our attention on other conditions corresponding to a lower postshock pressure. As far as the FIRE II probe is concerned, higher altitude and then higher-Mach-number trajectory points have to be considered. Indeed, local pressure and temperature are lower and the total density behind the shock front is also lower. Then, the collision frequency is lower and the role of radiation can be more significant. The high-altitude (HA) conditions studied in the present section correspond to $z = 76$ km at an elapsed time $t = 1634.0$ s from the launch of the FIRE II probe, where its velocity is $u_0 = 11.3$ km $\cdot$ s^{-1} (cf. Table 5). Therefore, the upstream Mach number is $\mathscr{M}_0 = 40.4$.

Figure 14 illustrates the spatial profiles obtained in this case for the temperatures T_A, T_e, $T_{v,1}$, $T_{v,2}$, $T_{v,3}$, $T_{v,4}$, and $T_{v,5}$. In the vicinity of the shock front, T_A is higher than in the LA conditions because the Mach number $\mathscr{M}_0$ is much higher. The postshock density is lower by one order of magnitude with respect to the LA conditions. The concomitant reduction of the collision frequency induces a shift in the downstream direction of the temperatures profiles and of the dissociation and ionization phases put forward previously. Table 6 gives numerical information on the related shift. Except a strong increase in $T_{v,3}$, the vibrational temperature curves are quite similar to the ones plotted in Fig. 2. The final state is obtained for $x \approx 9 \times 10^{-2}$ m. To characterize this state, we have performed a calculation without radiative elementary processes. The results are not modified. We have also calculated the spatial profile of the total energy of the flow per unit volume. This profile is quite uniform. We can conclude that the flow finally reaches an equilibrium state like for the LA conditions at a lower Mach number.

Since the results of the LA and HA conditions are very similar, we have chosen to illustrate their main differences by a unique table instead of showing unnecessary figures. Table 6 gives the x position of some significant events in the flow. We clearly point out the decrease in the total density, therefore, in the collision frequency from

Table 6 Comparison of x positions of some significant events in the flow between LA and HA test cases (see Table 5)

	LA conditions		HA conditions	
Event	Value	x position, m	Value	x position, m
T_A maximum decrease	48,600 K	4.3×10^{-5}	55,300 K	5.4×10^{-4}
$T_{v,1}$ maximum	21,900 K	4.6×10^{-5}	22,500 K	5.5×10^{-4}
T_e - $T_{v,1}$ coupling	11,900 K	2.8×10^{-4}	11,200 K	6.3×10^{-3}
T_e - $T_{v,1}$ - T_A coupling	11,200 K	6.5×10^{-4}	10,200 K	1.7×10^{-2}
$T_{v,3}$ maximum	24,700 K	1.1×10^{-4}	60,200 K	1.6×10^{-3}
$T_{v,4}$ maximum	13,800 K	5.1×10^{-5}	25,100 K	6.3×10^{-4}
T_e - $T_{v,1}$ - T_A - $T_{v,2}$ - $T_{v,3}$ - $T_{v,4}$ - $T_{v,5}$ coupling	10,600 K	7.3×10^{-3}	10,100 K	8.9×10^{-2}
T_{exc}[N] minimum	2,600 K	5.9×10^{-5}	2,500 K	9.0×10^{-4}
Onset of the dissociation phase	$D_d = 10^{-10}$	4.8×10^{-6}	$D_d = 10^{-10}$	6.7×10^{-5}
Onset of the ionization phase	$D_i = 10^{-10}$	1.8×10^{-5}	$D_i = 10^{-10}$	2.2×10^{-4}
$[N_2^+]$ maximum	4.5×10^{20} m^{-3}	7.5×10^{-5}	3.2×10^{19} m^{-3}	1.0×10^{-3}
$d[N(^4S^o_{3/2})]/dx$ maximum	5.7×10^{27} m^{-4}	5.2×10^{-5}	2.9×10^{25} m^{-4}	6.3×10^{-4}
dn_e/dx maximum	2.9×10^{26} m^{-4}	6.5×10^{-5}	1.5×10^{24} m^{-4}	8.7×10^{-4}

the LA to the HA conditions by the shift of these events to higher x positions. In spite of a decrease in the total density of one order of magnitude, the radiative processes again play a minor role.

As for the LA case (see end of Sec. III.A.5), we can conclude on the conditions at the edge of the boundary layer when the first part of the shock layer and the boundary layer are separately modeled. This edge is located at $x \approx 3.5 \times 10^{-2}$ m from the shock front in the present HA conditions [68]. Since equilibrium is reached at $x \approx 9 \times 10^{-2}$ m, the edge of the boundary layer therefore departs from equilibrium.

The work reported in this paper has two main perspectives. The first perspective concerns the validation of the CoRaM-N_2. From this point of view, comparisons should be performed with experimental results carried out at a high Mach number, mainly thinking to the ones obtained in the electric arc shock tube wind tunnel of NASA [69]. This comparison requires the elaboration of a specific radiative module deriving spectra from the spatial profiles of the excited species number densities. This elaboration is in progress. At a lower Mach number, former experimental results will be analyzed, such as the ones reported by Byron [17], Appleton et al. [18], Cary [70], Kewley and Hornung [71], and Hanson and Baganoff [72]. This validation will confirm the global relevance of this specific N_2 chemistry. The case of the FIRE II flight has been studied, and therefore the case of an entry taking place in the Earth's atmosphere. Of course, oxygen obviously plays a significant role, since its dissociation energy is lower than the one of nitrogen. In addition, the ionization channel is globally different owing to the formation of the NO^+ molecular ions by associative ionization $N + O \rightarrow NO^+ + e^-$ [21,73]. In the objective of a complete study of the FIRE II flight experiment, air mixtures have to be considered.

As a result, the second important perspective is the implementation of the CR model CoRaM-AIR in our one-dimensional flow, numerical code in an Eulerian approach. This CR model is based on CoRaM-N_2 and deals with shock layers produced during entries into the Earth's atmosphere or during shock tube experiments [35]. As for CoRaM-N_2, the model is vibrationally specific on the electronic ground state of the main molecules, and it is electronically specific for atoms, molecules, and ions. The objectives are the realistic prediction of the dissociation, the ionization, and the excitation of the flow. Another CR model dedicated to Martian atmospheric entries, called CoRaM-MARS, has also been elaborated and will be implemented in the one-dimensional flow code in the same Eulerian approach.

IV. Conclusions

The postshock relaxation of nitrogen flows in medium- and strong-Mach-number conditions has been thoroughly studied in this paper. The analysis of this relaxation has been performed by implementing the collisional-radiative model for N_2 in a one-dimensional flow, numerical code based on an Eulerian approach. This CR model takes into account 1) the vibrational states of the ground electronic state of N_2, 2) the excited electronic states of N_2, 3) the electronic states of N and N^+, and 4) free electrons in thermochemical nonequilibrium, assuming that electrons and heavy particles are in Maxwellian equilibrium at T_e and T_A, respectively. The collisional and radiative elementary processes involving the resulting 157 individual states for atomic and molecular species and electrons have cross sections or rate coefficients derived from literature. The set of forward and backward rate coefficients contains about 40,000 data. The shock front is considered as a discontinuity across which the jump of properties is treated using the classical Rankine–Hugoniot equations.

Two test cases have been discussed. They concern the flight of the well-known FIRE II probe, which took place in 1965 in the framework of the Apollo program. They correspond to the trajectory points at the altitudes $z = 54$ km and $z = 76$ km at Mach numbers of 32.0 and 40.4, respectively. Molecules crossing the shock front are first vibrationally excited. Then, they are dissociated. This dissociation phase is immediately followed by an ionization phase. During the dissociation phase, the vibrational distribution is far from being Boltzmanian. The dissociation mainly concerns the vibrational levels close to the dissociation limit, the density of which is underpopulated with respect to equilibrium owing to a strong collisional pumping. These results validate the adopted approach, which is based on a state-to-state modeling of the vibrational processes. As far as ionization is concerned, a similar behavior is observed for atomic levels close to the ionization limit. The thorough analysis of the influence of the elementary processes has pointed out the significant role played by N atoms and electrons in the dissociation and ionization phases, respectively. The highest molecular and atomic excitation is observed when the electron and N densities present the most significant gradients. Despite a reduction of one order of magnitude in the collision frequency from the first to the second case, the radiation does not play a significant role. This reduction is clearly observed, since the spatial profiles are shifted to x positions farther from the shock front.

Acknowledgments

The authors acknowledge the French Spatial Agency Centre National d'Etudes Spatiales. The research leading to these results has partially received funding from the European Community's Seventh Framework Program (FP7/2007-2013) under grant agreement no. 242311. The authors also acknowledge V. Laporta for the data related to vibrational excitation and dissociation rate coefficients of $N_2(X, v)$ under electron impact.

References

[1] Anderson, J. D., *Hypersonic and High Temperature Gas Dynamics*, McGraw–Hill, New York, 1989, pp. 483–502.

[2] Druguet, M.-C., "Prediction of the Flow Field over an Orbiter Entering the Mars Atmosphere," *Shock Waves*, Vol. 20, No. 3, 2010, pp. 251–261. doi:10.1007/s00193-009-0242-6

[3] Armenise, I., Capitelli, M., and Gorse, C., "Nitrogen Nonequilibrium Vibrational Distributions and Non-Arrhenius Dissociation Constants in Hypersonic Boundary Layers," *Journal of Thermophysics and Heat Transfer*, Vol. 12, No. 1, 1998, pp. 45–51. doi:10.2514/2.6300

[4] Bourdon, A., and Bultel, A., "Numerical Simulation of Stagnation Line Nonequilibrium Airflows for Reentry Applications," *Journal of Thermophysics and Heat Transfer*, Vol. 22, No. 2, 2008, pp. 168–177. doi:10.2514/1.33144

[5] Lamet, J.-M., Babou, Y., Rivière, P., Perrin, M.-Y., and Soufiani, A., "Radiative Transfer in Gases under Thermal and Chemical Nonequilibrium Conditions: Application to Earth Atmospheric Re-Entry," *Journal of Quantitative Spectroscopy and Radiative Transfer*, Vol. 109, No. 2, 2008, pp. 235–244. doi:10.1016/j.jqsrt.2007.08.026

[6] Panerai, F., and Chazot, O., "Characterization of Gas/Surface Interactions for Ceramic Matrix Composites in High Enthalpy, Low Pressure Air Flow," *Materials Chemistry and Physics*, Vol. 134, Nos. 2–3, 2012, pp. 597–607. doi:10.1016/j.matchemphys.2012.03.036

[7] Doroshenko, V. M., Kudryavtsev, N. M., and Smetanin, V. V., "Equilibrium of Internal Degrees of Freedom of Molecules and Atoms in Hypersonic Flight in the Upper Atmosphere," *Teplofizika Vysokikh Temperatur*, Vol. 29, No. 5, 1991, pp. 1013–1027.

[8] Park, C., "Review of Chemical-Kinetic Problems of Future NASA Missions, I: Earth Entries," *Journal of Thermophysics and Heat Transfer*, Vol. 7, No. 3, 1993, pp. 385–398. doi:10.2514/3.431

[9] Park, C., Howe, J. T., Jaffe, R. L., and Candler, G. V., "Review of Chemical-Kinetic Problems of Future NASA Missions, II: Mars Entries," *Journal of Thermophysics and Heat Transfer*, Vol. 8, No. 1, 1994, pp. 9–23. doi:10.2514/3.496

[10] Johnston, C. O., "Nonequilibrium Shock-Layer Radiative Heating for Earth and Titan Entries," Ph.D. Dissertation, Virginia Polytechnic Inst. and State Univ., Blacksburg, VA, 2006.

[11] Capitelli, M., Colonna, G., Pietanza, L. D., and D'Ammando, G., "Coupling of Radiation, Excited States and Electron Energy Distribution Function in Non Equilibrium Hydrogen Plasmas," *Spectrochimica Acta, Part B: Atomic Spectroscopy*, Vols. 83–84, May–June 2013, pp.1–13. doi:10.1016/j.sab.2013.03.004

[12] Bourdon, A., Annaloro, J., Bultel, A., Capitelli, M., Colonna, G., Guy, A., Magin, T. E., Munafò, A., Perrin, M.-Y., and Pietanza, L. D., "Reduction of State-to-State to Macroscopic Models for Hypersonics,"

Open Plasmas Physics Journal, Vol. 7, 2014, pp. 60–75.
doi:10.2174/1876534301407010060

[13] Annaloro, J., Morel, V., Bultel, A., and Omaly, P., "Global Rate Coefficients for Ionization and Recombination of Carbon, Nitrogen, Oxygen, and Argon," *Physics of Plasmas*, Vol. 19, No. 7, 2012, Paper 073515.
doi:10.1063/1.4737147

[14] Domingo, P., Bourdon, A., and Vervisch, P., "Study of a Low Pressure Nitrogen Plasma Jet," *Physics of Plasmas*, Vol. 2, No. 7, 1995, pp. 2853–2862.
doi:10.1063/1.871184

[15] Bultel, A., Chéron, B., and Vervisch, P., "Measurement of the Ground State and Metastable Atomic Nitrogen Number Density in a Low-Pressure Plasma Jet," *Plasma Sources Science and Technology*, Vol. 4, No. 4, 1995, pp. 597–605.
doi:10.1088/0963-0252/4/4/011

[16] Colonna, G., Pietanza, L. D., and Capitelli, M., "Recombination-Assisted Nitrogen Dissociation Rates Under Nonequilibrium Conditions," *Journal of Thermophysics and Heat Transfer*, Vol. 22, No. 3, 2008, pp. 399–406.
doi:10.2514/1.33505

[17] Byron, S., "Shock-Tube Measurement of the Rate of Dissociation of Nitrogen," *The Journal of Chemical Physics*, Vol. 44, No. 4, 1966, pp. 1378–1388.
doi:10.1063/1.1726870

[18] Appleton, J. P., Steinberg, M., and Liquornik, D. J., "Shock-Tube Study of Nitrogen Dissociation using Vacuum-Ultraviolet Light Absorption," *Journal of Chemical Physics*, Vol. 48, No. 2, 1968, pp. 599–608.
doi:10.1063/1.1668690

[19] Byron, S., "Measurement of the Rate of Dissociation of Oxygen," *Journal of Chemical Physics*, Vol. 30, No. 6, 1959, pp. 1380–1392.
doi:10.1063/1.1730209

[20] Matthews, D. L., "Interferometric Measurement in the Shock Tube of the Dissociation Rate of Oxygen," *Journal of Chemical Physics*, Vol. 2, No. 2, 1959, pp. 170–178.
doi:10.1063/1.1705908

[21] Bultel, A., Chéron, B. G., Bourdon, A., Motapon, O., and Schneider, I. F., "Collisional-Radiative Model in Air for Earth Re-Entry Problems," *Physics of Plasmas*, Vol. 13, No. 4, 2006, Paper 043502.
doi:10.1063/1.2194827

[22] Panesi, M., Magin, T., Bourdon, A., Bultel, A., and Chazot, O., "Fire II Flight Experiment Analysis by Means of a Collisional-Radiative Model," *Journal of Thermophysics and Heat Transfer*, Vol. 23, No. 2, 2009, pp. 236–248.
doi:10.2514/1.39034

[23] Panesi, M., Magin, T. E., Bourdon, A., Bultel, A., and Chazot, O., "Electronic Excitation of Atoms and Molecules for the FIRE II Flight Experiment," *Journal of Thermophysics and Heat Transfer*, Vol. 25, No. 3, 2011, pp. 361–374.
doi:10.2514/1.50033

[24] Munafò, A., Lani, A., Bultel, A., and Panesi, M., "Modeling of Non-Equilibrium Phenomena in Expanding Flows by Means of a Collisional-Radiative Model," *Physics of Plasmas*, Vol. 20, No. 7, 2013, Paper 073501.
doi:10.1063/1.4810787

[25] Panesi, M., Babou, Y., and Chazot, O., "Predictions of Non-Equilibrium Radiation: Analysis and Comparison with EAST Experiments," *40th Thermophysics Conference*, AIAA Paper 2008-3812, 2008.

[26] Armenise, I., Esposito, F., and Capitelli, M., "Dissociation-Recombination Models in Hypersonic Boundary Layer Flows," *Chemical Physics*, Vol. 336, No. 1, 2007, pp. 83–90.
doi:10.1016/j.chemphys.2007.05.015

[27] Laporta, V., Celiberto, R., and Wadhera, J. M., "Theoretical Vibrational-Excitation Cross Sections and Rate Coefficients for Electron-Impact Resonant Collisions Involving Rovibrationally Excited N_2 and NO Molecules," *Plasma Sources Sciences and Technology*, Vol. 21, No. 5, Paper 055018, 2012.
doi:10.1088/0963-0252/21/5/055018

[28] Armenise, I., Capitelli, M., Colonna, G., and Gorse, C., "Non-equilibrium Vibrational Kinetics in the Boundary Layer of Re-Entering Bodies," *Journal of Thermophysics and Heat Transfer*, Vol. 10, No. 3, 1996, pp. 397–405.
doi:10.2514/3.803

[29] Esposito, F., Armenise, I., and Capitelli, M., "$N - N_2$ State to State Vibrational-Relaxation and Dissociation Rates Based on Quasiclassical Calculations," *Chemical Physics*, Vol. 331, No. 1, 2006, pp. 1–8.
doi:10.1016/j.chemphys.2006.09.035

[30] Capitelli, M., Ferreira, C. M., Gordiets, B. F., and Osipov, A. I., *Plasma Kinetics in Atmospheric Gases*, Springer–Verlag, Berlin, 2000, pp. 167–191.

[31] Capitelli, M., and Celiberto, R., "Electron-Molecule Cross Sections for Plasma Applications: the Role of Internal Energy of the Target," *Novel Aspects of Electron-Molecule Collisions*, edited by Becker, K. H., World Scientific Publishing, Singapore, 1998, pp. 283–323.

[32] Capitelli, M., Celiberto, R., Eletskii, A., and Laricchiuta, A., "Electron-Molecule Dissociation Cross-Sections of H_2, N_2 and O_2 in Different Vibrational Levels," *Atomic and Plasma-Material Interaction Data for Fusion IAEA*, Vol. 9, 2001, pp. 47–64.

[33] Kosarim, A. V., Smirnov, B. M., Capitelli, M., Celiberto, R., Petrella, G., and Laricchiuta, A., "Ionization of Excited Nitrogen Molecules by Electron Impact," *Chemical Physics Letters*, Vol. 414, No. 3, 2005, pp. 215–221.
doi:10.1016/j.cplett.2005.08.012

[34] Lino da Silva, M., Guerra, V., and Loureiro, J., "Two-Temperature Models for Nitrogen Dissociation," *Chemical Physics*, Vol. 342, Nos. 1–3, 2007, pp. 275–287.
doi:10.1016/j.chemphys.2007.10.010

[35] Annaloro, J., "Modèles Collisionnels-Radiatifs Appliqués aux Situations D'entrée Atmosphérique Martienne et Terrestre," Ph.D. Dissertation, CORIA, Univ. de Rouen, France, 2013, (in French).

[36] Teulet, P., Sarrette, J.-P., and Gomes, A.-M., "Calculation of Electron Impact Inelastic Cross Sections and Rate Coefficients for Diatomic Molecules. Application to Air Molecules," *Journal of Quantitative Spectroscopy and Radiative Transfer*, Vol. 62, No. 5, 1999, pp. 549–569.
doi:10.1016/S0022-4073(98)00129-0

[37] Bultel, A., and Annaloro, J., "Elaboration of Collisional-Radiative Models for Flows Related to Planetary Entries into the Earth and Mars Atmospheres," *Plasma Sources Science and Technology*, Vol. 22, No. 2, 2013, Paper 025008.
doi:10.1088/0963-0252/22/2/025008

[38] Uyrova, I. U., and Ivanov, B. E., *Cross Sections for Scattering of Electrons by Atmospheric Gases*, Nauka, Leningrad, 1989, pp. 47–65.

[39] Brunger, M. J., and Buckman, S. J., "Electron-Molecule Scattering Cross-Sections. I. Experimental Techniques and Data for Diatomic Molecules," *Physics Reports*, Vol. 357, Nos. 3–5, 2002, pp. 215–458.
doi:10.1016/S0370-1573(01)00032-1

[40] Itikawa, Y., "Cross Sections for Electron Collisions with Nitrogen Molecules," *Journal of Physical and Chemical Reference Data*, Vol. 35, No. 1, 2006, pp. 31–53.
doi:10.1063/1.1937426

[41] Ristić, M. M., Vojnović, M., Poparić, G. B., and Belić, D. S., "Rate Coefficients for Electron Impact Excitation of the $a^3\Pi$ State of CO," *Chemical Physics*, Vol. 405, Sept. 2012, pp. 16–21.
doi:10.1016/j.chemphys.2012.05.018

[42] Drawin, H. W., *Collision and Transport Cross Sections*, European Atomic Energy Community EUR-CEA-FC 383, Rome, 1966.

[43] Morel, V., Bultel, A., and Chéron, B. G., "Modeling of Thermal and Chemical Non-Equilibrium in a Laser-Induced Aluminum Plasma by Means of a Collisional-Radiative Model," *Spectrochimica Acta, Part B: Atomic Spectroscopy*, Vol. 65, Nos. 9–10, 2010, pp. 830–841.
doi:10.1016/j.sab.2010.08.002

[44] Park, C., "Assessment of a Two-Temperature Kinetic Model for Dissociating and Weakly Ionizing Nitrogen," *Journal of Thermophysics*, Vol. 2, No. 1, 1988, pp. 8–16.

[45] Lotz, W., "Electron-Impact Ionization Cross-Sections and Ionization Rate Coefficients for Atoms and Ions from Hydrogen to Calcium," *Zeitschrift für Phyzik*, Vol. 216, No. 3, 1968, pp. 241–247.
doi:10.1007/BF01392963

[46] Park, J. T., Shoonover, D. R., and York, G. W., "Cross Section for Excitation of the Fourth Positive Band System in Carbon Monoxide by 20–120 keV Protons," *Physical Review A: General Physics*, Vol. 2, No. 6, 1970, pp. 2304–2308.
doi:10.1103/PhysRevA.2.2304

[47] Bhadra, K., and Ghosh, A. S., "1s–3d Excitation of Atomic Hydrogen by Electron and Proton Impact," *Physical Review Letters*, Vol. 26, No. 13, 1971, pp. 737–739.
doi:10.1103/PhysRevLett.26.737

[48] Drawin, H. W., "Influence of Atom-Atom Collisions on the Collisional-Radiative Ionization and Recombination Coefficients of Hydrogen Plasmas," *Zeitscrift für Physik*, Vol. 225, No. 5, 1969, pp. 483–493.
doi:10.1007/BF01392775

[49] Starik, A. M., Titova, N. S., and Arsentiev, I. V., "Comprehensive Analysis of the Effect of Atomic and Molecular Metastable State Excitation on Air Plasma Composition behind Strong Shock Waves," *Plasma Sources Sciences and Technology*, Vol. 19, No. 1, 2010, Paper 015007.
doi:10.1088/0963-0252/19/1/015007

[50] Kossyi, I. A., Kostinsky, A. Yu., Matveyev, A. A., and Silakov, V. P., "Kinetic Scheme of the Non-Equilibrium Discharge in Nitrogen-

Oxygen Mixtures," *Plasma Sources Sciences and Technology*, Vol. 1, No. 3, 1992, pp. 207–220.
doi:10.1088/0963-0252/1/3/011

[51] Kim, Y. K., and Desclaux, J.-P., "Ionization of Carbon, Nitrogen, and Oxygen by Electron Impact," *Physical Review A: General Physics*, Vol. 66, July 2002, Paper 012708.

[52] Peterson, J. R., Le Padellec, A., Danared, H., Dunn, G. H., Larsson, M., Larson, A., Peverall, R., Stromholm, C., Rosen, S., af Ugglas, M., and van der Zande, W. J., "Dissociative Recombination and Excitation of N_2^+: Cross Sections and Product Branching Ratios," *Journal of Chemical Physics*, Vol. 108, No. 5, 1998, pp. 1978–1988.
doi:10.1063/1.475577

[53] Chauveau, S., "Constitution de Bases de Données Spectroscopiques Relatives à un Plasma D'air. Application au Calcul de Transfert Radiatif," Ph.D. Dissertation, EM2C, École Centrale Paris, Châtenay-Malabry, France, 2001 , (in French).

[54] Holstein, T., "Imprisonment of Resonance Radiation in Gases," *Physical Review*, Vol. 72, No. 12, 1947, pp. 1212–1233.
doi:10.1103/PhysRev.72.1212

[55] Cornette, E. S., "Forebody Temperatures and Calorimeter Heating Rates Measured during Project FIRE II Reentry at 11.35 Kilometers per Second," NASA TM-X-1305, 1966.

[56] Boyd, I. D., Chen, G., and Candler, G. V., "Predicting Failure of the Continuum Fluid Equations in Transitional Hypersonic Flows," *Physics of Fluids*, Vol. 7, No. 1, 1995, pp. 210–219.
doi:10.1063/1.868720

[57] Din, F., and Burn, I., "Departures from Dalton's and Amagat's Laws," *Transactions of the Faraday Society*, Vol. 61, 1965, pp. 1351–1363.
doi:10.1039/tf9656101351

[58] Brown, P. N., Byrne, G. D., and Hindmarsch, A. C., "VODE: A Variable-Coefficient ODE Solver," *SIAM Journal on Scientific and Statistical Computing*, Vol. 10, No. 5, 1989, pp. 1038–1051.
doi:10.1137/0910062

[59] Shi, Y., Green, W. H., Wong, H.-W., and Oluwole, O. O., "Accelerating Multi-Dimensional Combustion Simulations Using GPU and Hybrid Explicit/Implicit ODE Integration," *Combustion and Flame*, Vol. 159, No. 7, 2012, pp. 2388–2397.
doi:10.1016/j.combustflame.2012.02.016

[60] Sissenwine, N., Dubin, M., and Wexler, H., "The U.S. Standard Atmosphere, 1962," *Journal of Geophysical Research*, Vol. 67, No. 9, 1962, pp. 3627–3630.
doi:10.1029/JZ067i009p03627

[61] Kentzer, C. P., "Quasilinear Form of Rankine–Hugoniot Jump Conditions," *AIAA Journal*, Vol. 24, No. 4, 1986, pp. 691–693.
doi:10.2514/3.9332

[62] Gross, R. A., "Strong Ionizing Shock Waves," *Reviews of Modern Physics*, Vol. 37, No. 4, 1965, pp. 724–743.
doi:10.1103/RevModPhys.37.724

[63] Peigin, S., Kazakov, V., Druguet, M.-C., Séror, S., and Zeitoun, D. E., "Three-Dimensional Thermochemical Nonequilibrium Viscous Flow over Blunt Bodies with Catalytic Surface," *AIAA Journal*, Vol. 39, No. 4, 2001, pp. 626–636.
doi:10.2514/2.1355

[64] Colonna, G., Pietanza, L. D., and D'Ammando, G., "Self-Consistent Collisional-Radiative Model for Hydrogen Atoms: Atom–Atom Interaction and Radiation Transport," *Chemical Physics*, Vol. 398, June 2012, pp. 37–45.
doi:10.1016/j.chemphys.2011.06.019

[65] Huber, K. P., and Herzberg, G., *Molecular Spectra and Molecular Structure, IV: Constants of Diatomic Molecules*, van Nostrand, New York, 1979, pp. 412–420.

[66] Loftus, A., and Krupenie, P. H., "The Spectrum of Molecular Nitrogen," *Journal of Physical and Chemical Reference Data*, Vol. 6, No. 1, 1977, pp. 113–307.
doi:10.1063/1.555546

[67] Farrenq, R., Rossetti, C., and Guelachvili, G., "Experimental Rovibrational Populations of CO up to $v = 40$ from Doppler-Limited Fourier Spectra of the Sequences $\Delta v = 1$, 2 and 3 Emitted by a Laser Type Source," *Chemical Physics*, Vol. 92, Nos. 2–3, 1985, pp. 389–399.
doi:10.1016/0301-0104(85)85033-3

[68] Lamet, J.-P., "Transferts Radiatifs dans les Écoulements Hypersoniques de Rentrée Atmosphérique Terrestre," Ph.D. Dissertation, EM2C, École Centrale Paris, Châtenay-Malabry, France, 2009, (in French).

[69] Cruden, B. A., Martinez, R., Grinstead, J. H., and Olejniczak, J., "Simulation Vacuum Ultraviolet Through Near IR Absolute Radiation Measurement with Spatio-Temporal Resolution in an Electric Arc Shock Tube," *41st AIAA Thermophysics Conference*, AIAA Paper 2009-4240, 2009.

[70] Cary, B., "Shock-Tube Study of the Thermal Dissociation of Nitrogen," *Physics of Fluids*, Vol. 8, No. 1, 1965, pp. 26–35.
doi:10.1063/1.1761099

[71] Kewley, D. J., and Hornung, H. G., "Free-Piston Shock-Tube Study of Nitrogen Dissociation," *Chemical Physics Letters*, Vol. 25, No. 4, 1974, pp. 531–536.
doi:10.1016/0009-2614(74)85360-1

[72] Hanson, R. K., and Baganoff, D., "Shock-Tube Study of Nitrogen Dissociation Rates Using Pressure Measurements," *AIAA Journal*, Vol. 10, No. 2, 1972, pp. 211–215.
doi:10.2514/3.50082

[73] Motapon, O., Fifirig, M., Florescu, A., Waffeu-Tamo, F.-O., Crumeyrolle, O., Varin-Bréant, G., Bultel, A., Vervisch, P., Tennyson, J., and Schneider, I. F., "Reactive Collisions between Electrons and NO^+ Ions: Rate Coefficient Computations and Relevance for the Air Plasma Kinetics," *Plasma Sources Science and Technology*, Vol. 15, No. 1, 2006, pp. 23–32.
doi:10.1088/0963-0252/15/1/004